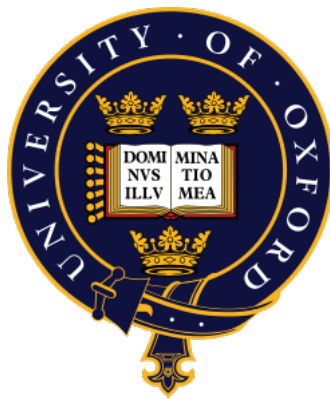


The Development of High Sensitivity
Spectroscopic Techniques for Remote Sensing of
Trace Gases in the Martian Atmosphere

First Year Report



Richard L. Passmore

Lincoln College

Atmospheric, Oceanic and Planetary Physics
University of Oxford

Supervisors: Dr. Neil E. Bowles
and Dr. Kevin M. Smith (Rutherford Appleton Laboratory)

August 2009

Abstract

Methane has been detected in the atmosphere of Mars by several research teams in the last few years. Ground-based observations (e.g. Krasnopolsky et al. [2004] and Mumma et al. [2009]) and space-based missions (e.g. the Planetary Fourier Transform spectrometer on Mars Express: Formisano et al., 2004) have reported low levels of methane gas (approximately 10ppb) in the Martian atmosphere. Methane detection is important as its presence could imply a biological origin. However, current results are at the instruments' lower limits of detection.

The work described in this report researches the viability of remote sensing using laser heterodyne radiometry (LHR) to detect methane in the Martian atmosphere. The LHR technique allows high spectral resolution (greater than 0.001 cm^{-1}) measurements over a narrow spectral range ($\sim 10 \text{ cm}^{-1}$). The advantages of such an instrument, including its compact lightweight design, over current remote sensing spectral instruments are discussed.

Contents

1	Introduction	1
2	Mars	4
2.1	Thermal Structure of the Martian Atmosphere	6
2.2	Dust in the Martian Atmosphere	7
2.3	The Water Cycle on Mars	9
3	Methane	11
3.1	The Methane Molecule	11
3.2	Methane on Earth	12
3.3	Methane on Mars	13
3.3.1	Possible Sources of the Martian Methane	13
3.3.2	Possible Sinks of the Martian Methane	14
3.3.3	The Search for Methane on Mars	16
4	Radiative Transfer Calculations	21
4.1	Simulating a Simple Gas Cell	22
4.2	Simulating a Single Path Atmosphere	23
4.3	Simulating the Martian Atmosphere	25
4.3.1	The COSPAR Database	25
4.3.2	The Mars Climate Database	31
4.3.3	Adding Dust to the Model	35
5	Laser Heterodyne Radiometry for Remote Sensing of Martian Methane	42
5.1	Fourier Transform Spectroscopy	42
5.2	Laser Heterodyne Radiometry	43
5.2.1	Heterodyne Detection	43
5.2.2	Instrument Sensitivity	44
5.2.3	Comparing the LHR with a Fourier Transform Spectrometer	44
5.3	Quantum Cascade Laser LHRs	45
5.4	Simulating Mars in the Laboratory	46
6	Conclusions	48
7	Future Work	49
	Bibliography	52

A Equations	58
B A Summary of Mars Missions	59

Chapter 1

Introduction

Mars has been the subject of human fascination and mystery for millennia. However, over the past 50 years our knowledge of the Red Planet has been transformed by numerous successful space missions. From the Mariner probes to the Mars Phoenix lander, we have had a close-up view like never before. Although, there have unfortunately been many disappointments (e.g. Mars Climate Orbiter and the Beagle 2 lander). Yet despite these failures, man continues to return, more invigorated than before.

In recent years, the possible discovery of methane in the atmosphere of Mars, by remote infrared spectroscopy, has led many to speculate as to its origin. Previous work on methane detection is discussed in chapter 3 of this report. Some attribute past hydrothermal activity and cometary impacts to the levels of methane seen today [Krasnopolsky et al., 2004], while some theorise Martian bacteria or microorganisms to be responsible [Boston et al., 1992]. Whatever the cause, all agree that higher resolution measurements of the atmosphere, preferably from Mars orbit, need to be carried out to confirm the presence of the gas. So far, Fourier transform spectrometers have been used in studies; both from telescopes on Earth, and satellites in orbit around Mars. Earth based instruments have the advantage of high spectral resolution (e.g. CSHELL on the IRTF has a resolution of 0.076 cm^{-1}), but they have poor, if any, spatial resolution. The other disadvantage is the presence of terrestrial absorption lines in the measured spectrum, which have to be removed. Instruments aboard probes around Mars have the advantage of proximity to the Martian surface, the absence of telluric absorption and good spatial resolution. However the current generation of instruments only have moderate spectral resolution (e.g. the FTS on Mars Express has a resolution of 1.3 cm^{-1}). This is a result of the instrument's limitation due to size and mass restrictions. To achieve a high spectral resolution in an instrument such as Fourier transform spectrometer (FTS), a large optical path difference is required, which results in a complex and high mass instrument. For example, the mass of the MIPAS instrument on the ESA ENVISAT satellite in low Earth orbit, which has a spectral resolution of 0.035 cm^{-1} , is 327 kg [Endemann, 1999], where as the PFS instrument on Mars Express is 30.9 kg [Formisano et al., 2005]. The reason a high resolution FTS has not already been sent to Mars is because the scientific case has not been made that justified the large, and very heavy, instrument.

This project aims to research the potential of remote sensing of the Martian atmosphere using Laser Heterodyne Radiometry (LHR) to detect methane. LHRs have the benefit of high sensitivity, high spatial resolution and ultrahigh spectral resolution down to, and even below, 0.001 cm^{-1} . During the retrieval of terrestrial atmospheric ozone profiles, Weidmann et al. [2007b] concluded that a carefully selected specific high resolution microwindow provided as much information as a medium resolution radiometer covering a broad spectral range. This major advantage favours the development of a compact and lightweight LHR instrument over the current large and heavy Fourier transform spectroradiometers.

The new, enabling technology at the heart of the LHR is the use of a Quantum Cascade Laser (QCL) as the local oscillator. The radiation from the local oscillator is mixed with that from the scene, in this case, the Martian atmosphere. QCLs are an ideal local oscillator for this instrument as they provide the necessary optical power and have spectral purity in the kHz to MHz range [Weidmann et al., 2007b]. They also have the advantage of continuous frequency tuning over a specific spectral window, and are extremely compact and reliable devices.

This report focuses on the published work on Martian methane detection, and attempts to reproduce the results. Atmospheric simulations have been carried out recreating known conditions on Mars (chapter 4). Spectra have been produced using the Oxford Planetary radiative transfer modelling code, RADTRANS [Irwin et al., 1997], using profiles of Mars obtained from the COSPAR and the Mars Climate Database (MCD). These databases contain information about temperature, pressure and the volume mixing ratios of the major gases present in the atmosphere of Mars. From their data, Krasnopolsky et al. [2004] and Formisano et al. [2004] concluded a CH_4 mixing ratio of 10 ppb. Therefore this value was used when simulating spectra. The strongest fundamental bands of CH_4 are the ν_4 band centred around 1306 cm^{-1} and the ν_3 band centred around 3019 cm^{-1} . Formisano et al. [2004] concentrated on the ν_3 band as the signal-to-noise ratio (SNR) of the Planetary Fourier Spectrometer (PFS) on-board Mars Express is much greater in the 3000 cm^{-1} region. As a result the work in this report focuses mainly on this CH_4 fundamental band. Spectra were produced at high (0.005 cm^{-1}) and low resolutions (1 cm^{-1}) and with varying levels of atmospheric dust, with and without the presence of methane. The results, detailed in chapter 4, show CH_4 observed at 3018 cm^{-1} . The maximum radiance at this peak was then plotted as a function of spectral resolution. The noise equivalent power of the PFS and LHR are compared to the RADTRANS simulations and conclude the LHR instrument is an ideal candidate for atmospheric spectral studies.

The work on the LHR will be performed at the Molecular Spectroscopy Facility (MSF) at the Rutherford Appleton Laboratory (RAL). The instrument will first be tested to determine its ability to measure methane gas transmission through small gas cells. A Martian atmosphere will then be replicated which will include aerosols to mimic typical dust levels. Data from the LHR will be processed and wavelength calibrated transmission spectra will be produced. The instruments sensitivity and discrimination of overlapping spectral features will

be analysed. A conclusion will be made whether methane can be detected using the LHR as well, or better, than a Fourier transform spectrometer. If successful, the potential for remote sensing measurements of the Martian atmosphere will be evaluated.

Chapter 7 discusses the plans for future work relating to this project.

Chapter 2

Mars

Mars has been a source of fascination for many cultures throughout history. The planet is named after Mars, the Roman God of War. The ancient Egyptians referred to Mars as Har Decher ‘The Red One’. It was known in India as Lohitanga meaning ‘Red-bodied’, and referred to in Chinese culture as the Fire Star. Astronomers have observed Mars for centuries: Christiaan Huygens made early sketches in 1659, and in the late 19th and early 20th century Percival Lowell published drawing of what he perceived to be Martian canals, captivating the public’s imagination. In 1877 American astronomer Asaph Hall discovered the two moons of Mars, Phobos and Deimos, which are small and irregularly shaped.

Billions of years ago, Mars may have possessed a mild and humid climate, with rivers and oceans, like that of present day Earth [Forget et al., 2008]. However, today it is a cold planet (with surface temperatures averaging < 200 K) with a very thin atmosphere (< 10 mbar). During the history of the planet, Mars lost its primitive atmosphere. The volume of the atmosphere was reduced as a result of several processes: Erosion under the action of solar winds and photochemical reactions with UV radiation. Violent meteoritic impacts could have ejected much of Mars’ early atmosphere into space, with the planet’s low gravity unable to retain the gases. The chemical loss of carbon dioxide, in the presence of liquid water, formed carbonates on the surface, and atmospheric CO_2 condensed at the planet’s poles. The pressure on the surface of Mars is now between 100 to 150 times lower than the Earth. Planetary and atmospheric parameters for Mars, and their corresponding terrestrial values, are displayed in Table 2.1.

Until the Mariner 4 mission in 1965, it was assumed that the atmosphere of Mars was similar to that of Earth, dense and consisting mainly of nitrogen [Forget et al., 2008]. However it was revealed by a radio-occultation measurement to be to be tenuous and that the dense appearance is a result of dust suspended in the atmosphere [Chamberlain and McElroy, 1966]. It was determined that the mean surface pressure is approximately 6 millibars and that the atmosphere is in fact composed of 95% carbon dioxide. The Viking probes in 1976 discovered the other main components of the atmosphere to be nitrogen and argon, with small amounts of oxygen. The SPICAN spectrometer aboard Mars Express measured small amounts of ozone and water vapour, and the Planetary Fourier Spectrometer (PFS) detected traces of methane. Observations of Martian methane have

	Mars	Earth
Equatorial Radius	3396 km	6378 km
Mass	6.42×10^{23} kg	5.976×10^{24} kg
Mean Density	3.95×10^3 kg m ⁻³	5.52×10^3 kg m ⁻³
Surface Gravity	3.72 m s ⁻²	9.81 m s ⁻²
Surface Pressure	600 Pa (variable)	101,300 Pa
Surface Temperature	140 – 300 K	230 – 315 K
Mean Orbital Radius	227.9×10^6 km	149.6×10^6 km
Orbital Period	687 days	365.25 days
Mean Orbital Velocity	24.13 km s ⁻¹	29.79 km s ⁻¹
Inclination of the Orbital Plane	1.85°	0.0°
Orbital Eccentricity	0.0934	0.0167
Rotation Period	24.62 hours	24 hours
Planetary Obliquity	25.19°	23.45°

Table 2.1: *Planetary and atmospheric parameters for Mars and Earth [Read and Lewis, 2004]*

also been made from Earth [e.g. Krasnopolsky et al., 2004, Mumma et al., 2009], and will be discussed in chapter 3. The principle constituents of the atmosphere of Mars are shown in Table 2.2.

4.4 billion years ago Mars had a global magnetic field, formed by convection within the liquid core. Since then the core has cooled and convection halted, switching off the planet’s ‘dynamo’ [Forget et al., 2008]. Mars Global Surveyor (MGS) in 1997 measured the magnetic field of the ionosphere, and detected local magnetic anomalies.

In its orbit, Mars reaches its nearest point to the Earth, known as opposition, about every 26 months. The most favourable of these occur approximately every 15 Earth years. Mars can be seen from Earth with the naked eye. Its apparent magnitude reaches -2.9 [Williams, 2004]. Mars has an average opposition distance from Earth of 78 million km and a closest approach of 55.7 million km. In 2003, Mars made its closest approach to Earth in nearly 60,000 years, and this opportunity was used to launch Mars Express, which reached the planet within 7 months.

Gas	Concentration
CO ₂	95.32%
N ₂	2.7%
Ar	1.6%
O ₂	0.13%
CO	0.07%
H ₂ O	Approx. 0.03%

Table 2.2: *Principle constituents of the atmosphere of Mars [Forget et al., 2008]*

2.1 Thermal Structure of the Martian Atmosphere

Most of the mass of Mars' atmosphere is confined to the troposphere (0–50 km). In this layer the temperature falls off rapidly with increasing altitude. This trend can be seen in figure 2.1. An 'ozone layer' like the one in Earth's atmosphere, is absent from Mars. Between 60 and 120 km the thermal profile stabilises due to the absorption of solar radiation in the near IR by carbon dioxide. Above 120 km, the thermosphere, the few molecules present are exposed to the most energetic photons of intense UV radiation, which dissociates them and warms them significantly [Forget et al., 2008].

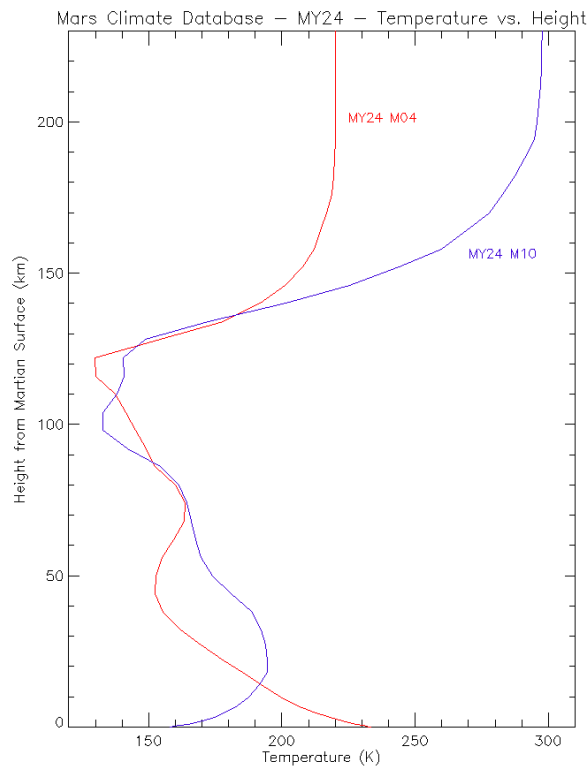


Figure 2.1: *Vertical temperature profile of the Martian atmosphere. The data were obtained from the Mars Climate Database for the northern hemisphere (at coordinates 48.8°N , 0°E). The red profile represents a Martian summer and blue a Martian winter. MY24 Month 4 (M04) $L_s = 90^{\circ} - 120^{\circ}$. MY24 Month 10 (M10) $L_s = 300^{\circ} - 330^{\circ}$.*

2.2 Dust in the Martian Atmosphere

In July 1976, Viking 1 transmitted the first colour pictures from the surface of Mars. The dust covering the Martian surface ranges in diameter from a few micrometres to hundreds of micrometres [Forget et al., 2008]. The finest of these particles are lifted by the wind to form dust storms [Sagan and Bagnold, 1975]. Observations of atmospheric dust tell us that the year can be divided into two distinct periods: a ‘clear season’ during northern spring and summer, and a ‘dust season’ during autumn and winter, when great dust storms occur. These seasonal dust variations can be seen in figure 2.2.

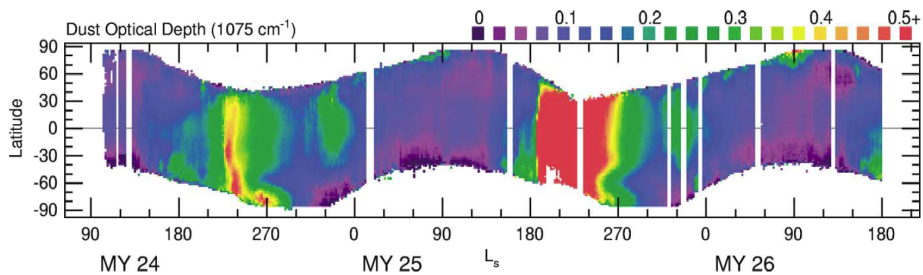


Figure 2.2: Variation in the amount of dust in the Martian atmosphere as a function of latitude. Dust optical depth at 1075 cm^{-1} scaled to an equivalent 6.1 mbar pressure surface (to remove the effect of topography). Purple indicates a clear atmosphere, and red signifies a thick dusty atmosphere. Measured by the Thermal Emission Spectrometer (TES) aboard Mars Global Surveyor (MGS). The largest data gaps were caused by solar conjunction and various times when the MGS spacecraft went into contingency mode [Smith, 2004].

Insolation is at its peak during southern spring, when Mars is closest to the Sun. At this time of year a large number of regional dust storms are common in the southern hemisphere. The severity of the dust storms varies from year to year. Mars Year 24 in figure 2.2 shows dust measurements for the Martian year lasting from 1999 to 2000 when only a few regional dust storms were observed. Contrast that with the autumn of Mars Year 25 (MY 25), from 2001 to 2002, which shows a planet-wide storm. For many months, almost the whole of Mars was obscured in dust. This was first observed in 1956, when Mars’ orbit brought the planet closer to Earth than usual. When NASA’s Mariner 9 probe arrived at Mars in November 1971, the planet’s surface was again hidden by a global dust storm and the start of mapping had to be delayed until the dust had settled [Toon et al., 1977]. Figure 2.3 shows the Mars global storm of 2001, imaged by the Mars Orbiter Camera (MOC) on Mars Global Surveyor (MGS). It illustrates how atmospheric dust conditions on Mars can vary on short timescales. A clear atmosphere was observed in mid-June, 2001, and within 6 weeks, a global dust storm had encompassed the entire planet.

Martian Dust is important to consider when simulating an atmosphere using RADTRANS and also in the laboratory. Dust must be taken into account as it has a notable effect on the observed spectrum. RADTRANS simulations of the Martian atmosphere that incorporate a dust model are investigated in section 4.3.3.

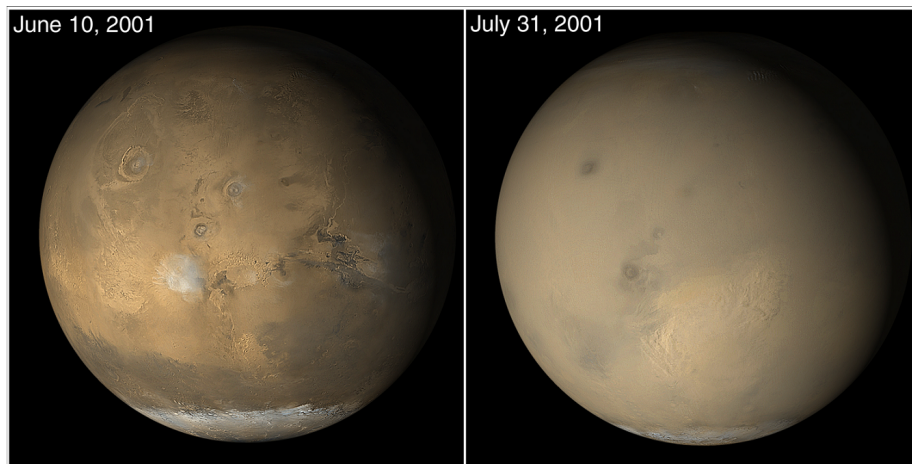


Figure 2.3: *Images of the Mars 2001 global dust storm taken by the Mars Orbiter Camera (MOC) on Mars Global Surveyor (MGS).*

The Martian Soil

The Martian soil is dry and granular and inefficient at storing heat: its ‘thermal inertia’ is very low compared to the surface of the Earth with its oceans. The Viking probes (1 & 2) and Pathfinder determined the most abundant constituent of the Martian soil is Silica (Silicon Dioxide, SiO_2) at 43%. Second most abundant is Ferric Oxide (Rust) [Forget et al., 2008].

2.3 The Water Cycle on Mars

This section discusses Martian atmospheric water vapour. This is important because H_2O has strong spectral features around the same areas as the fundamental methane bands, especially the $\text{CH}_4 \nu_3$ band at $3.3 \mu\text{m}$. H_2O can contaminate the methane signal, making detection difficult, particularly at low resolutions.

The annual water cycle on Mars as observed by the Thermal Emission Spectrometer (TES) on Mars Global Surveyor (MGS) is shown figure 2.4. The quantity of water vapour in the Martian atmosphere is expressed in ‘precipitable microns’¹. The results show a strong maximum in the summer of the northern hemisphere. A peak water column of approximately 100 pr- μm was attained in each of the two Martian years observed poleward of 80°N latitude at $L_s = 110^\circ - 120^\circ$ [Smith, 2002]. The maximum column abundance during the southern mid-summer reached a maximum of 50 pr- μm . Low water abundances are observed during fall and winter at middle and high latitudes of both hemispheres. Figure 2.5 is a plot the change in seasonal atmospheric water vapour, for the northern and southern hemisphere. Recent work by Fouchet et al. [2007] using data from the PFS/LW on Mars Express concludes a substantially drier water cycle. They measure a maximum water column at high latitudes in northern summer of ~ 60 pr- μm . They identify a flaw in the TES data, but advise that it still be used because it is a more complete dataset, after a revision to lower the column abundances is performed.

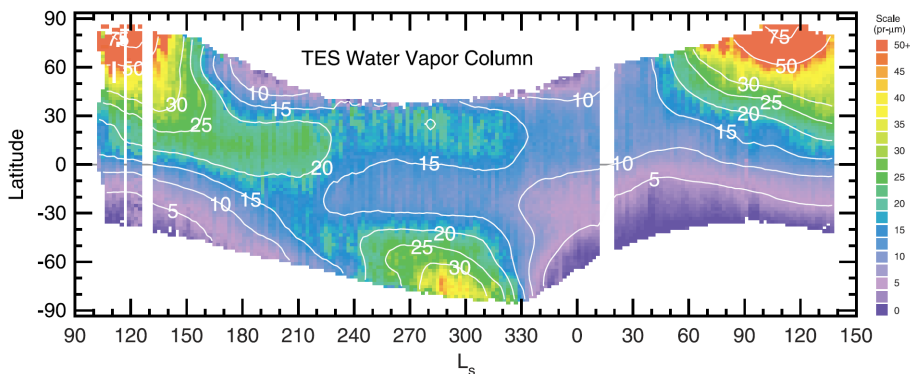


Figure 2.4: *The column abundance of water vapour as a function of season (L_s) and latitude as observed by TES. Water vapour abundance is shown for the Mars Global Surveyor (MGS) mapping period between $L_s = 104^\circ$, March 1st, 1999 and $L_s = 137^\circ$, March 28th, 2001. Results include only daytime data (local time $\sim 14:00$) where the surface temperature is >220 K. Results have been zonally averaged into bins that are 2° wide in latitude and 2° wide in L_s . The total water column integrated perpendicularly from the surface to infinity is shown. The data has not been topographically scaled. Contours show a smoothed representation of the results [Smith, 2002].*

¹A precipital micron (pr- μm) is a measure of the water depth in a column of atmosphere if it could be condensed at the surface. $1 \text{ pr-}\mu\text{m} = 3.34 \times 10^{18} \text{ cm}^{-2}$ [Wolfram Research]

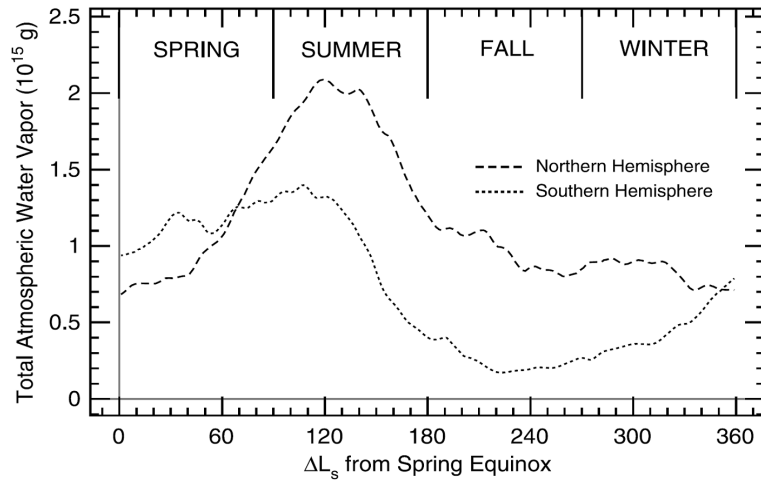


Figure 2.5: *The annual cycle of water vapour on Mars as observed by the Thermal Emission Spectrometer (TES) on Mars Global Surveyor (MGS). The total amount of atmospheric water vapour is plotted for each season for the northern hemisphere (dashed line), the southern hemisphere (dotted line), during one Martian year (March 1999 to March 2001). Seasons are expressed as ΔL_s (solar longitude) from spring equinox ($L_s = 0^\circ$ for the northern hemisphere and $L_s = 180^\circ$ for the southern hemisphere) [Smith, 2002].*

The Martian Poles

The north pole is a vast glacier, 1000 km across, made up of water ice, sediments and dust [Forget et al., 2008]. During the summer months, the ice warms up, but does not melt to a liquid state, as the pressure on Mars is too low. Instead it sublimates directly into the atmosphere. This is the source of the increased water vapour observed in the summer in the TES data. The water vapour is transported in the atmospheric circulation towards more southern latitudes by the large Martian Hadley cell. In contrast, at the south pole, water condenses but never leaves. The average temperature is -130°C , and water can only exist in this region as ice. A permanent layer of carbon dioxide ice covers the southern polar cap, and locks in the water.

Mariner 4 (1966) revealed that during the Martian winters at the poles, down to a latitude of 50° , the surface is covered in a layer of carbon dioxide ice, a few tens of centimetres thick. This occurs at a temperature of around -125°C and is a result of the atmosphere partly solidifying at one of the two polar caps. The north CO_2 ice cap has a mid-winter diameter of 5000 km [Forget et al., 2008]. In the spring when the temperature increases, the CO_2 sublimates and the ice cap recedes polewards. In the northern hemisphere in summer the CO_2 ice evaporates completely and the permanent water ice cap is revealed. The following autumn, the CO_2 cap returns. The southern winter is longer than the northern winter, due to the eccentricity of Mars' orbit. The southern CO_2 ice cap does not fully retreat, and there is always a region where the CO_2 does not sublimate. Also, the atmospheric pressure is lower during the southern winter because more CO_2 condenses out.

Chapter 3

Methane

3.1 The Methane Molecule

Methane (CH_4) is a polyatomic, spherical top molecule with four identical moments of inertia. It absorbs and radiates in the infrared by the excitation of the bonds between constituent atoms. This leads to internal vibrational and rotational transitions, resulting in a characteristic spectrum. CH_4 consists of five atoms, resulting in nine degrees of freedom corresponding to nine normal vibrations: four stretching modes and five bending modes [Bowles, 2003]. The stretching modes consist of the ν_1 non-degenerate symmetric stretch (centred at 2917 cm^{-1}) and ν_3 triply degenerate anti-symmetric stretch (3019 cm^{-1}). The bending modes consist of the ν_2 doubly degenerate (1534 cm^{-1}) and the ν_4 triply degenerate (1306 cm^{-1}) [The HITRAN Database]. However, only the ν_4 and ν_3 bands are infrared active, these are shown in figure 3.1, and are the focus of methane detection for this project. The central vibration frequencies can be split into three branches; a central Q branch, which has no change in its total angular momentum quantum number ($\Delta J = 0$), the P branch to the left of the Q branch, which has a change in rotational quantum number of $\Delta J = -1$, and the R branch to the right, which has a change in rotational quantum number of $\Delta J = +1$ [Bowles, 2003]. The observed PQR structure is a result of the simultaneous vibration and rotation of the molecule.

The following information on the molecule is listed in the HITRAN database: The molecular mass of CH_4 is 16.0426 g/mol , it has a freezing point of $-182.5 \text{ }^\circ\text{C}$ and a boiling point of $-161.5 \text{ }^\circ\text{C}$.

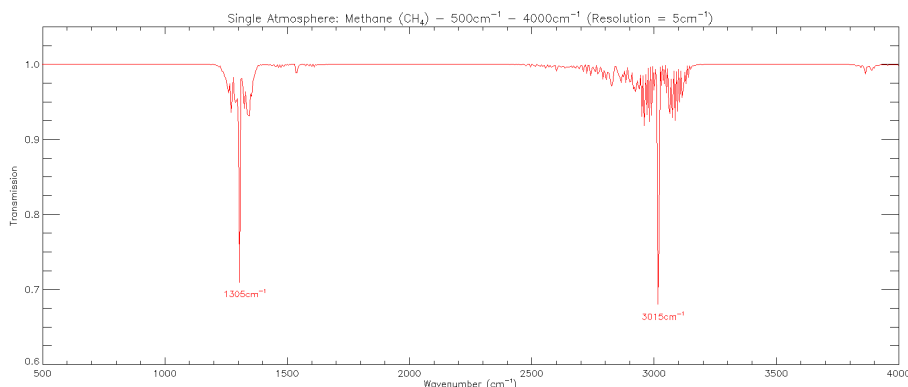


Figure 3.1: A synthetic methane spectrum showing the main fundamental bands, calculated using RADTRANS and using data from the HITRAN 2004 database, covering the $500 - 4000 \text{ cm}^{-1}$ spectral range, at a resolution of 5 cm^{-1} . Calculations were performed on a simulated gas cell, of path length 30 cm, containing 10 ppb of CH_4 at a pressure of 10 mbar and at a temperature of 150 K.

Spectral Line Strength

The intensity of the spectral lines are determined by several factors: the transition probability of the system, the population of energy states and the path length of the sample; the greater the distance the radiation beam traverses, the more energy will be absorbed from it [Banwell and McCash, 1994].

Spectral Line Shape

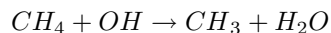
The line shape determines the wavenumber dependence of a spectral feature in the vicinity of the line position. When a spectrometer resolves lines, they do not appear as infinitely narrow features, but are instead spread over a finite wavenumber range. There are several mechanisms that are responsible for the line shape: One is the natural line broadening due to the molecule's fundamental quantum mechanical nature, and the other is a function of the environment of the molecules (Doppler and Lorentz broadening) [Hanel et al., 2003]. Doppler broadening is temperature dependent and is due to the molecule's translational motion and distortions induced by the presence of other molecules. Lorentz (collision) broadening is a function of both pressure and temperature [Beer, 1992] (see appendix A for equations).

3.2 Methane on Earth

Methane sources on Mars are currently the topic of much speculation. On Earth however, there is much conclusive data on the topic. The first unambiguous detection of methane in Earth's atmosphere was that of Migeotte [1948], who observed its infrared absorption bands in the solar spectrum. Methane is the most abundant organic chemical in Earth's atmosphere [Cicerone and Oremland, 1988]. The global average amount of methane in the atmosphere in 2005 was measured at $1,774.62 \pm 1.22$ ppb [Forster et al., 2007].

There are many sources of methane on Earth, the most significant of these include: Microorganisms called methanogens produce large amounts of methane as they respire; they are responsible for anaerobic decomposition in wetlands and irrigated rice paddies [Matthews and Fung, 1987]. Methane is also produced by enteric fermentation in ruminants (animals), decomposition in landfills, and a contribution by termites. Abiogenic sources of methane include: Natural gas production and consumption, the mining and processing of coal, biomass burning, and the release from the breakdown of clathrates.

Methane lifetime on Earth is approximately 9 to 10 years [Rowland, 1985]. Methane is destroyed predominantly in the troposphere by the chemical reaction with the hydroxyl radical OH:



The OH radical is extremely short-lived in the troposphere, reacting primarily with CO or CH₄ on time scales of 10 seconds or less [Fung et al., 1991].

3.3 Methane on Mars

Since the discovery of methane in the atmosphere of Mars, its origin has proved a mystery. Volcanic activity, comet impacts, and the presence of methanogenic microbial life forms have been considered as sources [Krasnopolsky et al., 2004, Boston et al., 1992, Weiss et al., 2000]. Whether biological or geological, methane on Mars has become an important topic of investigation. The total photochemical loss of CH₄ in the Martian atmosphere is equal to $2.2 \times 10^5 \text{ cm}^{-2} \text{ s}^{-1}$, or 270 tons per year, with a lifetime of approximately 340 years [Krasnopolsky et al., 2004], and as a result would require a continuous CH₄ source to maintain current levels. The methane lifetime on Mars is long enough to allow for winds and diffusion to mix the gas into the atmosphere homogeneously, so the large deviations in observed methane levels over the planet were unexpected [Mumma et al., 2009]. This suggests that the CH₄ originates from localised sources.

3.3.1 Possible Sources of the Martian Methane

Atreya et al. [2007] argue that volcanoes are most likely not responsible, as they have been extinct for hundreds of millions of years. Also, if they were the source of the methane, they would also have expelled vast amounts of sulphur dioxide (SO₂), and no evidence of sulphur compounds in the Martian atmosphere has been found. Therefore, the volcanic origin of the methane is doubtful. The calculated average delivery of methane by cometary impacts, meteorites, and interplanetary dust equates to less than 6% of the lost methane [Krasnopolsky et al., 2004]. Lyons et al. [2005] discuss the production of methane by fluid-rock interaction in the Martian crust. Its detection could indicate active magma on the planet. They conclude that the low temperature alteration of basaltic crust by carbon-bearing hydrothermal fluid can produce a CH₄ flux of 1×10^7 moles per year. It has been suggested that methane could form in liquid water under a layer of permafrost by serpentinization of olivine, assuming the presence of CO₂ [Oze and Sharma, 2005, Atreya et al., 2007].

Krasnopolsky [2006] acknowledges that geological sources of methane are possible, but concludes that the lack of current volcanism, hydrothermal activity,

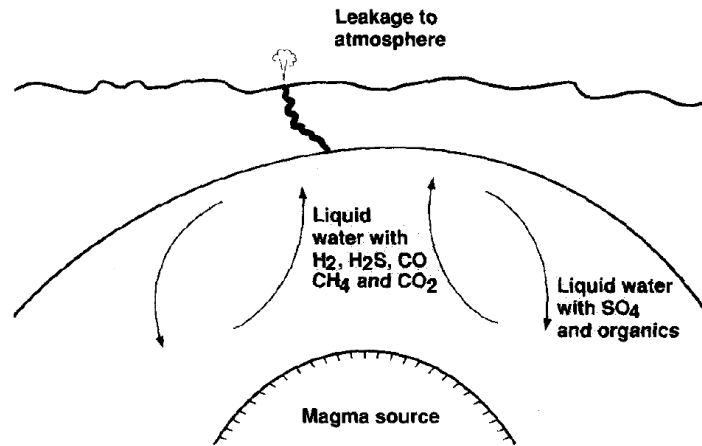
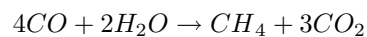
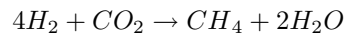


Figure 3.2: *Illustration of a possible hydrothermal habitat on Mars. The circulation of water is forced by the pressure of a temperature gradient [Clifford, 1991]. Reduced volcanic gases are carried upward while oxidized and organic materials are carried downward [Boston et al., 1992].*

hot spots, and the low levels of out-gassing from the interior limit these as the only source of the methane. The possibility of methane producing bacteria or microorganisms has been suggested by a number of authors [Boston et al., 1992, Weiss et al., 2000, Krasnopolsky et al., 2004]. Max and Clifford [2000] suggest methanogenic bacteria could be present in a possible liquid saline groundwater layer at a depth of around 6 km. The chemical reactions involved in microbe metabolism, from Atreya et al. [2007], are:



Boston et al. [1992] consider a possible scenario involving hydrothermal habitats below the Martian surface; an illustration is seen in figure 3.2. Methane is then released at localised sources at the surface, known as hot spots [Wong et al., 2003].

3.3.2 Possible Sinks of the Martian Methane

Methane is primarily broken down by photochemical reactions in the upper atmosphere. These reactions are listed in figure 3.3.

Reaction	Rate coefficient ($\text{cm}^3 \text{s}^{-1}$)	Column rate ($\text{cm}^{-2} \text{s}^{-1}$)	
$\text{CH}_4 + h\nu (1216 \text{ \AA}) \rightarrow \text{products}$	–	1.0×10^5	1.0×10^5
$\text{CH}_4 + \text{OH} \rightarrow \text{CH}_3 + \text{H}_2\text{O}$	$2.45 \times 10^{-12} \exp(-1775/T)$	1.0×10^5	1.2×10^4
$\text{CH}_4 + \text{O} \rightarrow \text{CH}_3 + \text{OH}$	$8.3 \times 10^{-12} (T/300)^{1.56} \exp(-4270/T)$	560	120
$\text{CH}_4 + \text{O}(^1\text{D}) \rightarrow \text{CH}_3 + \text{OH}$	1.5×10^{-10}	7.8×10^4	5×10^4
Total		2.8×10^5	1.6×10^5

Figure 3.3: *Reactions for the photochemical loss of methane in the Martian atmosphere. Column rates for the reactions are calculated using the photochemical models of Nair et al. [1994, Fig.15] and Krasnopolsky [1995, Fig.2a] in the left and right columns, respectively. The main process is photolysis by solar Lyman-alpha radiation. This occurs at around 80 km [Krasnopolsky et al., 2004].*

There is also research that suggests that methane concentrations decrease at regions of local dust storm activity. Studies performed by Farrell et al. [2006] demonstrate that Martian dust devils and large dust storms generate large-scale electric fields. These E-fields have the ability to produce major electron drift motions that are capable of dissociating any trace CH_4 in the ambient atmosphere, therefore acting as a sink of methane. Figure 3.4 shows the relationship between electrostatic field and methane destruction. As the E-field increases, the CH_4 destruction time geometrically decreases. For large E-fields the CH_4 destruction rate is approximately 1000 seconds.

Atreya et al. [2006] considers that at the surface, H_2O_2 could serve as a strong oxidiser that could accelerate the loss of methane from the atmosphere.

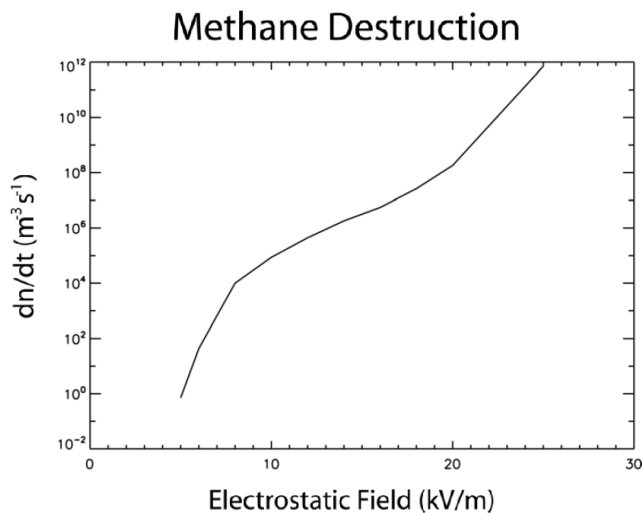


Figure 3.4: *Methane destruction as a function of electrostatic field, assuming a methane concentration of 10 ppb [Farrell et al., 2006].*

3.3.3 The Search for Methane on Mars

Martian methane has been a topic of interest for several authors over the last few years. A summary of their findings is discussed below:

Horn et al. [1972] placed an upper limit of CH_4 at 3.7 ppm, in their study of the ν_3 band using Mariner 6 and 7 infrared spectrometer data, and the Mariner 9 orbiter (1971) did not detect the IR absorption of methane at 1306 cm^{-1} , which resulted in an upper limit of 20 ppb Maguire [1977].

Krasnopolsky et al. [1997] indicated a potential detection of methane in the Martian atmosphere while observing Mars in the $2650 - 2800 \text{ cm}^{-1}$ spectral range during their search for HDO (Hydrogen Deuterium Oxide). They detected methane as a by-product of their search, with a measured concentration of 70 ± 50 ppb, which was below the 2σ limit of the instrument. Observations were conducted June 28th – 30th, 1988, using the Fourier Transform Spectrometer at the Kitt Peak National Observatory, Arizona.

Lellouch et al. [2000] observed Mars on July 31st, 1997 between $2.4 - 45 \mu\text{m}$ using the short-wavelength spectrometer on the ESA Infrared Space Observatory (ISO). They did not detect methane in its strong ν_3 band centred at $3.3 \mu\text{m}$, with an upper limit of 50 ppb.

Krasnopolsky et al. [2004] in January 1999, used the Fourier Transform Spectrometer (FTS) of the Canada-France-Hawaii Telescope, located near the Mauna Kea Observatory in Hawaii. They recorded the Martian spectrum between 2840 and 3020 cm^{-1} with a resolving power of 180,000 ($\Delta\nu = 0.016 \text{ cm}^{-1}$). They reported the detection of methane, after the summation of the 15 strongest CH_4 transitions, at a 3.7σ level. They concluded a CH_4 mixing ratio of 10 ± 3 ppb. This method of detection has the advantage of a very high spectral resolution. However limitations include the presence of terrestrial absorption lines and the lack of spatial resolution.

Formisano et al. [2004] observed Mars between January and February, and in May 2004, using the Planetary Fourier Spectrometer (PFS) on Mars Express to detect methane in the Martian atmosphere. The instrument has a spectral resolution of 1.3 cm^{-1} and a spatial resolution of about 10 km at pericentre. They concentrated on the ν_3 fundamental band as the SNR of the Mars Express PFS is much greater in the region around 3000 cm^{-1} . Data from 16 orbits were summed and used to calculate a mean CH_4 mixing ratio of 10 ± 5 ppb. Figure 3.5 shows a PFS spectrum of the $3000 - 3030 \text{ cm}^{-1}$ region that was studied, overlaid with simulated spectra containing varying amounts of CH_4 . There are advantages to using space based instruments to collect data, which include proximity to the Martian Surface and the absence of telluric absorption. However, disadvantages include only a moderate resolving power of 2300 ($\Delta\nu = 1.3 \text{ cm}^{-1}$) from the instrument which has a spectral sampling of 1 cm^{-1} . There was also a major dust storm in development during the measurement period that could have affected the retrievals.

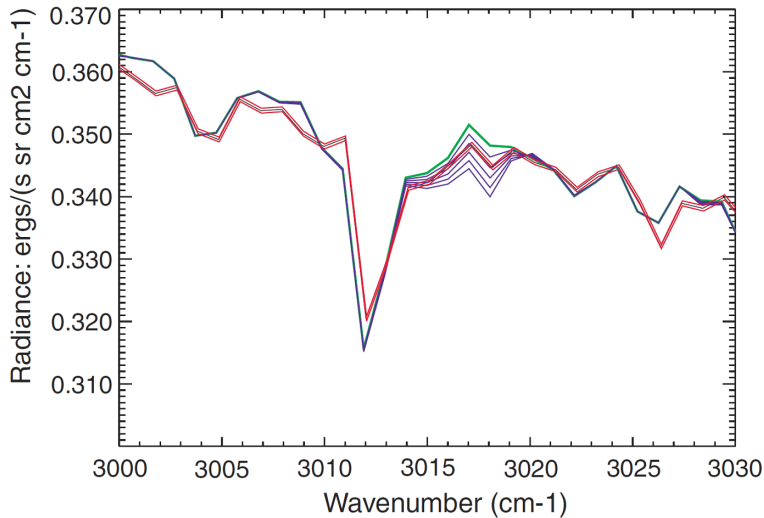


Figure 3.5: An averaged spectrum of the Martian atmosphere between 3000 – 3030 cm^{-1} recorded by the PFS on Mars Express between January–February 2004 (black curve), with $\pm 1\sigma$ confidence (red lines). The SNR is about 1300. Methane is identified at 3018 cm^{-1} . There are three water lines (at 3003.5, 3022, and 3026 cm^{-1}) and two solar lines (at 3012 and 3014 cm^{-1}). The continuum slope is due to water ice clouds in the atmosphere. The small peak at the left of the main solar line is due to instrumental response function. Also shown are simulated methane spectra computed at concentrations of 0 ppbv (green curve) and 10, 20, 30, 40, and 50 ppbv (violet curves). The simulated spectra have been computed for 6.7 mbar of CO_2 , including 350 ppm of H_2O , along with dust and water ice clouds. The temperature profile obtained from simultaneous measurements in the thermal radiation was used [Formisano et al., 2004].

Mumma et al. [2004] used CSHELL on The NASA Infrared Telescope Facility (IRTF), located on Hawaii’s Mauna Kea Observatory, in March 2003 and Phoenix (a near-IR spectrometer) on Gemini South, located in the Chilean Andes, in May 2003. CSHELL and Phoenix are cryogenic infrared echelle spectrographs [Greene et al., 1993, Hinkle et al., 1998]. A slit was situated along the central meridian of the disk and the spectra were recorded as a function of latitude. A partial mapping of the Martian disk was obtained as the planet rotated. The 3020 – 3040 cm^{-1} spectral range was observed with a spectral resolution higher than 10^4 (CSHELL has a resolution of 0.076 cm^{-1} [Wiedemann et al., 2001]). They detected large volumes of methane in two specific areas, both close to the equator, with Eastern longitudes of 300°, in March 2003, and about 60°, in May 2003. From the IRTF data, they concluded a maximum CH_4 mixing ratio of 250 ppb. From the data obtained at Gemini South, a value of 60 ppb CH_4 was established at the location of maximum intensity. This method has the advantage of high spectral resolution with some spatial resolution.

These observations provided only a tentative detection of methane on Mars. However, between January and March 2006, Mumma et al. [2009] observed localised sources of methane on Mars. They used high-dispersion IR spectrometers located at the Mauna Kea Observatory: CSHELL on IRTF and The Near

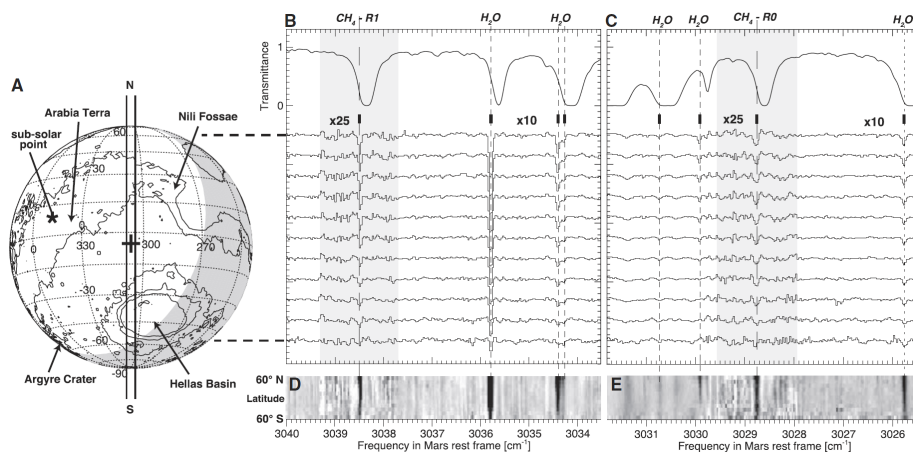


Figure 3.6: *Detections of CH_4 and water vapour on Mars on March 19th and 20th, 2003. (A) Mars is shown as it appeared at the mean time of the RO and R1 observations. The subsolar (*) and sub-Earth (+) points are marked, along with several prominent features. The entrance slit of the spectrometer was oriented north-south on Mars along the central meridian and is shown to scale. (B) Spectra taken on March 20th were extracted at 11 equal intervals (0.6 arc sec each) along the slit (ranging from 70°N to 70°S), after binning over longitudes 277° to 323°W . (C) Spectra taken on March 19 are binned over the longitude range from 289° to 335° . Spectral lines of H_2O (three lines, short dashes) and CH_4 (long dashes) are seen. (D and E) show residual intensities in a greyscale format, and show the spatial distribution of the gases with latitude [Mumma et al., 2009].*

Infrared Spectrometer (NIRSPEC) on Keck II. The spectrometers feature a long entrance slit that is held to the central meridian of Mars (figure 3.6A) while spectra are taken sequentially in time. Pixelated spectra were acquired simultaneously at neighbouring positions along the entire slit length for each observation, which provided 35 spectra at 0.2 arc second intervals when Mars' diameter was 7 arc seconds. The data were binned to provide latitudinally resolved spectra, and then in time (longitude) to improve the signal to noise ratio. These spectra are shown in figure 3.6B and 3.6C.

During Mars' northern midsummer, they detected a principle extended plume of methane, containing approximately 19,000 metric tons of CH_4 (Figure 3.7, profile d) with an estimated source strength greater than 0.6 kg per second. In Figure 3.8, Mumma et al. [2009] use their midsummer 2003 data to construct a high resolution map where CH_4 is particularly enhanced over several localised areas.

Simulations by Lefèvre and Forget [2009] attempt to recreate the localised methane sources observed by Mumma et al. [2009]. They conclude that an atmospheric lifetime of less than 200 days is necessary to reproduce the same local levels of detected methane. This results in a loss of CH_4 600 times faster than calculated by standard photochemistry in order to maintain the same amount of methane in the atmosphere.

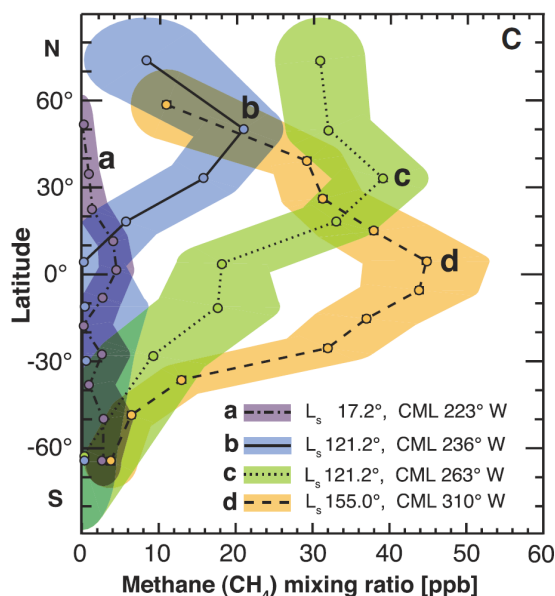


Figure 3.7: *Geographic and temporal variability of Martian methane. Latitudinal profiles of CH_4 mixing ratios for different longitudes and seasons are shown; the width of the colour band represents the $\pm 1\sigma$ confidence. The aerocentric seasons (L_s) are early northern spring (a: 17°), early northern summer (b and c: 122°), and late northern summer (d: 155°). Data is obtained from spectra centred at the indicated meridian longitude (CML) [Mumma et al., 2009].*

NASA’s Mars Science Laboratory (MSL) rover, planned for launch in 2011, will house instruments that will make dedicated measurements of methane over one Martian year. The onboard Analytical Laboratory is designed to achieve a more detailed investigation of biological habitability [Atreya et al., 2007].

Since the majority of the published CH_4 detection has been made in the ν_3 band, in order to compare with these authors’ work, this band has been the primary region for study during this report. Martian spectra have been produced using RADTRANS, concentrating on the $3000 - 3030 \text{ cm}^{-1}$ region. A study of the ν_4 band has also been carried out and the results are discussed in the next chapter.

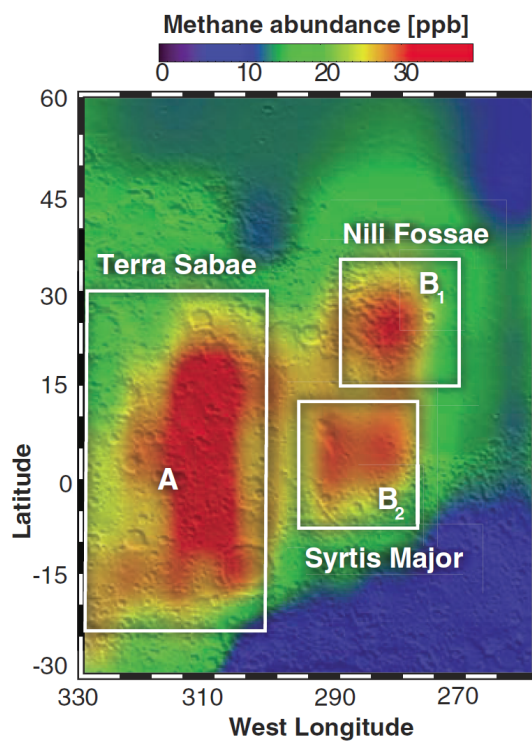


Figure 3.8: *High resolution map constructed from IR data from ground based observations of Mars in 2003. Regions are highlighted where methane appears noticeably localised in northern midsummer (A, B₁ and B₂) and their relationship to mineralogical and geomorphological domains [Mumma et al., 2009].*

Chapter 4

Radiative Transfer Calculations

Radiative transfer is the theory that permits the computation of the signal received at the input to the remote sensor in terms of the spectral radiance¹. This section describes the use of the RADTRANS [Irwin et al., 1997] software for the study of simulated atmospheres.

RADTRANS

If the temperature, pressure and composition of an atmosphere are known then radiative transfer theory can be used to model its spectrum. RADTRANS is a **R**adiative **T**ransfer modelling program used to study simulated planetary atmospheres. RADTRANS can simulate anything from a single gas atmosphere in a laboratory gas cell, to multi-gas multi-layer atmospheres with particle scattering. Both nadir or limb observations can be reproduced. The RADTRANS model calculates the transmission, absorption or thermal emission spectra of a gaseous path using one of three spectral models: Line-by-line, Band or Correlated-k. RADTRANS can also calculate multiple-scattered spectra. Depending on the spectral model selected, information is read in either from a line database, an averaged band parameter, or k-distribution table. The input files containing the atmospheric profiles include all the information needed to model the atmosphere of any planet. For this project the Mars atmospheric profiles used were obtained from the Committee on Space Research (COSPAR, the International Mars Reference Atmosphere). The profiles contain information about Martian atmospheric temperatures and pressures in relation to height from the surface. Also included are the atmospheric abundances of the major gases, in terms of their volume mixing ratio (vmr), present in Mars' atmosphere – CO₂, H₂O, O₂, CO, O₃. In order to simulate Martian spectra containing methane a concentration of 10 ppbv CH₄ was added to the Martian profiles. This amount of CH₄ was used as it was the mean mixing ratio Krasnopolsky et al. [2004] and Formisano et al. [2004] determined during their studies of the Martian atmosphere. The spectroscopic parameters containing the intensities and line positions of the peaks of the individual gases were taken from the

¹The units of radiance are: W cm⁻² sr⁻¹/cm⁻¹ [Beer, 1992]

HITRAN 2004 (High Resolution Transmission) database. HITRAN is a very comprehensive database used for calculating atmospheric molecular transmission and radiance from the microwave through to the UV region of the spectrum [Rothman et al., 2005].

4.1 Simulating a Simple Gas Cell

The simulated gas cells and atmospheres are defined in the input .pat file. This file contains information about the number and type of gases, including the volume mixing ratios of each, the pressure, the temperature, the region of the spectrum to calculate, and the spectral resolution. There are three parts to calculating and outputting a RADTRANS simulated spectrum. First, *Path*, which computes atmospheric absorber paths and outputs in the correct form to be read by *Radtrans*. It reads commands from the input path file with the extension .pat and produces an output driver file with the extension .drv. Next, *Radtrans* reads the .drv file and performs the spectral calculations. The line by line model was used to perform the *Radtrans* calculations, and the absorption line cut off was set at 35 cm^{-1} . DELV is a user selected value which defines the width of the square bins. *Radtrans* integrates the spectrum over DELV wide regions centred on the chosen wavenumber values. In order to cover the line wings from lines outside the spectral region, *Radtrans* uses VREL to extend the calculations beyond the minimum (VMIN) and maximum (VMAX) input wavenumbers. All lines outside of this modified range are then ignored during the calculations. Finally, *Pl_spec* reads in the binary data output from *Radtrans* and converts it to an ASCII file suitable for plotting using IDL [RADTRANS Manual].

The absorption spectrum of a gas cell containing methane was calculated over a wide spectral range ($500 - 4000\text{ cm}^{-1}$) at a low resolution (5 cm^{-1}) in order gain familiarity with RADTRANS and to identify the main fundamental bands of CH_4 (figure 3.1). The cell has a path length of 30 cm, this was chosen since this is typical of the short path gas cells used at RAL in their high-resolution spectrometers, and contains 10 ppb of CH_4 at a pressure of 10 mbar and a temperature of 150 K. The ν_4 (at 1305 cm^{-1}) and ν_3 (at 3015 cm^{-1}) bands, and their PQR structures, are clearly visible in the spectrum.

4.2 Simulating a Single Path Atmosphere

Following the simulations on a single gas in a cell, an atmosphere with a single layer was created. Mars-like conditions were taken into account when selecting the parameters. Figure 4.1 shows an absorption spectrum covering the $100 - 5000 \text{ cm}^{-1}$ spectral range at a resolution of 5 cm^{-1} . A simulated atmosphere at a pressure of 7 mbar, a temperature of 150 K, and a 100 km path length was chosen. It is composed of CO_2 (0.95321%), N_2 (0.04649%), H_2O (300 ppm) and CH_4 (10 ppb). This spectrum shows how difficult it is to identify methane in a Mars like atmosphere. The spectrum is dominated by CO_2 , and in the regions where CH_4 is located, there is a strong presence of H_2O vapour.

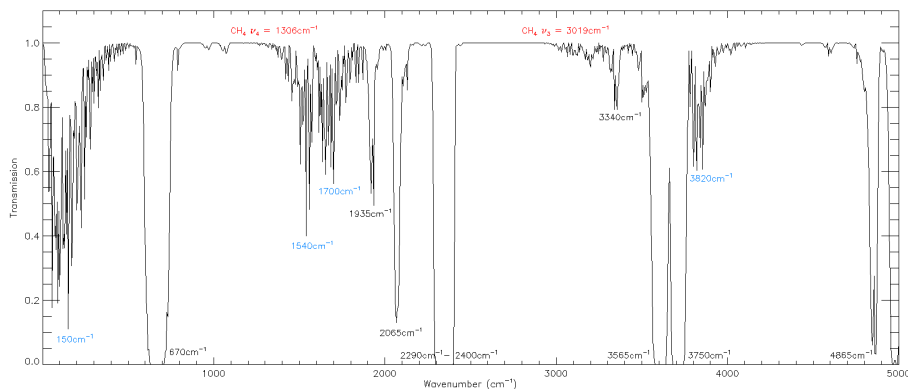


Figure 4.1: A RADTRANS spectrum from a simulated single atmosphere, of path length 100 km, containing CO_2 (0.95321%), N_2 (0.04649%), H_2O (300 ppm) & CH_4 (10 ppb) at a pressure of 7 mbar and at a temperature of 150 K. The spectral range is from $100 - 5000 \text{ cm}^{-1}$ at a resolution of 5 cm^{-1} . The CO_2 features are labelled in black, the water vapour in blue, and the indicated methane regions are in red.

In order to identify the CH_4 bands more clearly, narrower parts of the spectrum were chosen, and RADTRANS was re-run at a higher resolution. Figure 4.2 (A) is a spectrum from $1290 - 1320 \text{ cm}^{-1}$ centred on the ν_4 CH_4 band, and figure 4.2 (B) shows a spectrum from $3000 - 3030 \text{ cm}^{-1}$ highlighting the ν_3 CH_4 band. Both spectra have a resolution of 0.01 cm^{-1} , and are simulated in a single layer atmosphere of path length 50 km, at a pressure of 7 mbar and a temperature of 150 K. They contain 95% CO_2 , 0.046% N_2 , 350 ppm H_2O and 10 ppb CH_4 . Both spectra were also simulated without CH_4 , so a comparison could be made between an atmosphere containing 10 ppb CH_4 , and atmosphere containing none. The CH_4 has been highlighted in red from the background spectra. The blue absorption lines and labels indicate H_2O . These spectra show that at a high resolution, the CH_4 is distinguishable from the background H_2O vapour. The next section will focus on producing more comprehensive, mutli-layered atmospheric models for RADTRANS simulations.

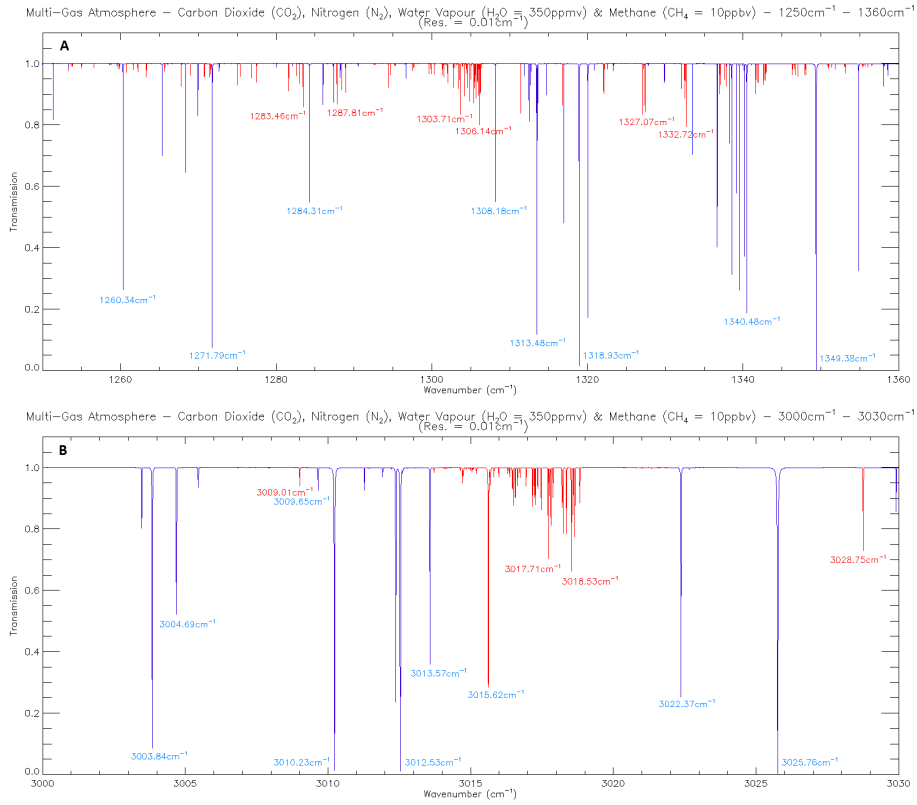


Figure 4.2: RADTRANS spectra from a simulated single atmosphere, of path length 50 km, containing CO₂ (0.95321%), N₂ (0.04649%), H₂O (350 ppm) & CH₄ (10 ppb) at a pressure of 7 mbar and at temperature of 150 K. (A) shows a spectrum in the 1290 – 1320 cm⁻¹ region and (B) shows a spectrum in the 3000 – 3030 cm⁻¹ region. Both spectra were calculated at a resolution of 0.01 cm⁻¹. The CH₄ features are highlighted and labelled in red. The blue absorption lines and labels indicate H₂O vapour.

4.3 Simulating the Martian Atmosphere

In order to simulate a planetary atmosphere, additional input information is required. Data regarding the Martian atmosphere needs to be supplied by splitting the atmosphere into a series of layers, each one defined as a function of altitude. The corresponding pressure, temperature and gas volume mixing ratios at each layer are supplied in the .prf input file, which is linked to the .pat file. The information about viewing geometry for the simulations is stored in the .pat file.

4.3.1 The COSPAR Database

The COSPAR International Mars Reference Atmosphere profile [Kliore, 1982] for northern summer provided the information needed to build a more comprehensive RADTRANS simulation. The profile contains 51 evenly separated vertical layers, every 2 km, from the surface to an altitude of 100 km. The data used to construct the COSPAR profile was obtained during the NASA Viking missions.

Figure 4.3 shows COSPAR spectra produced using RADTRANS at a resolution of 1 cm^{-1} . The simulated atmospheres contain CO_2 (0.95321%), O_2 (0.0013%), CO (700 ppm), H_2O (300 ppm), O_3 (120 ppb) and CH_4 (10 ppb). At the surface the atmospheric pressure is 6.36 mbar and the temperature is 214 K. The pressure decreases exponentially with altitude until it reaches almost 0 mbar at 100 km. The temperature decreases with a linear trend until it reaches 139 K at 100 km. The calculations in figure 4.3 were all performed in the nadir. Figure (A) covers the $500 - 5000 \text{ cm}^{-1}$ spectral range and figures (B) and (C) highlight the ν_4 and ν_3 CH_4 regions of the spectrum respectively. The blue spectra were producing using the COSPAR profile containing no CH_4 , and the red features that are overlaid indicate COSPAR spectra with added CH_4 (10 ppb). Within the $1290 - 1320 \text{ cm}^{-1}$ region, the ν_4 CH_4 band is visible, centred at 1306 cm^{-1} and in the $3000 - 3030 \text{ cm}^{-1}$ region, the ν_3 CH_4 band is visible, centred at 3018 cm^{-1} . Emission lines in the $1290 - 1320 \text{ cm}^{-1}$ region have a stronger radiance than the emission lines in the $3000 - 3030 \text{ cm}^{-1}$ region. But indications from these spectra suggest that the ν_3 CH_4 band, centred at 3018 cm^{-1} , would be easier for methane detection instead of the ν_4 CH_4 band, because it can be better distinguished from the background water vapour. The ν_3 peak sits between H_2O vapour lines as opposed to sitting on top of them like the ν_4 peak.

Higher resolution (0.005 cm^{-1}) RADTRANS calculations were performed on the ν_4 and ν_3 CH_4 regions using the COSPAR profiles. The $1290 - 1320 \text{ cm}^{-1}$ region is shown in figure 4.4, and the $3000 - 3030 \text{ cm}^{-1}$ region is shown in figure 4.5. They show an increase in radiance of between 10^1 and 10^2 . The CH_4 bands are now more prominent than they were at low resolution (1 cm^{-1}).

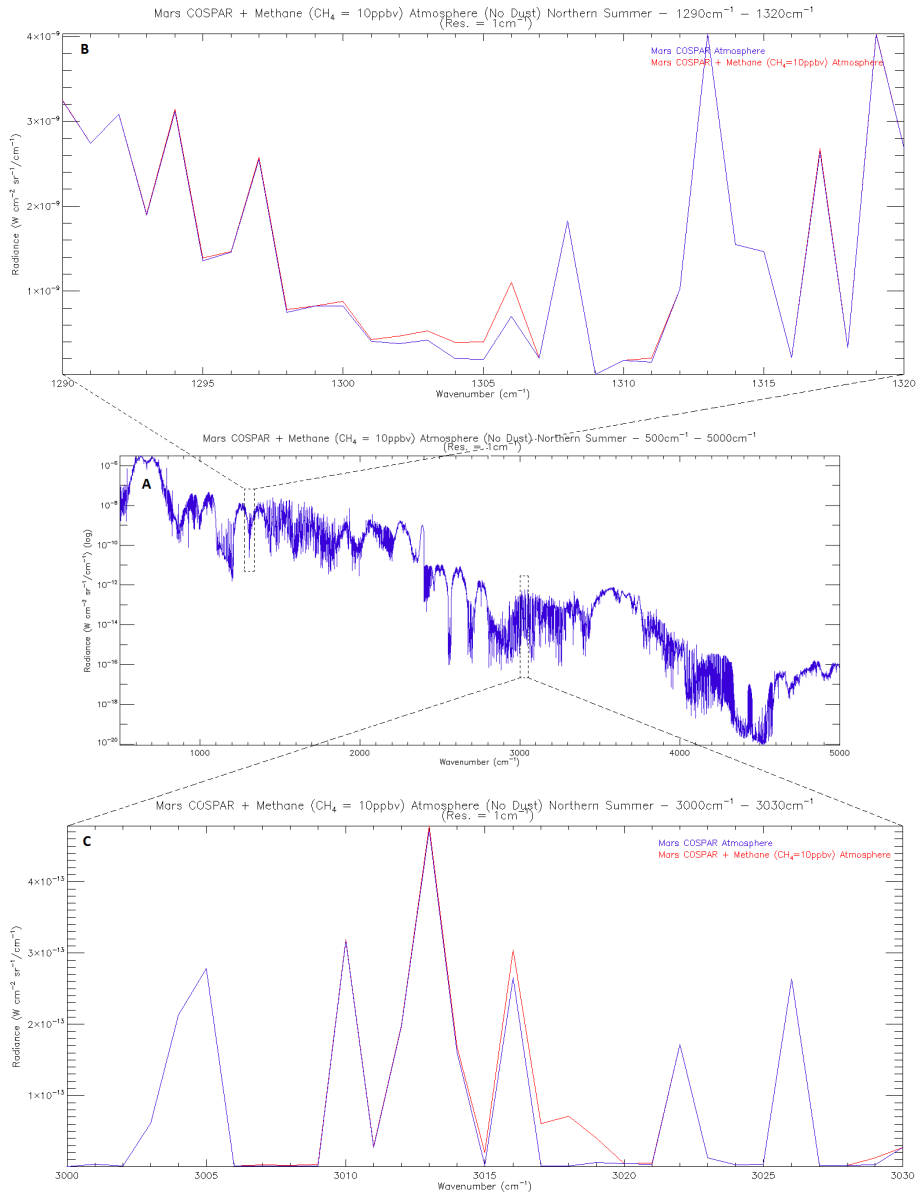


Figure 4.3: Spectra produced using RADTRANS with the COSPAR Mars profile. Spectra were calculated at a resolution of 1 cm^{-1} , in the nadir at a height of 100 km from the surface. (a) covers the $500 - 5000 \text{ cm}^{-1}$ spectral range. (b) covers the $1290 - 1320 \text{ cm}^{-1}$ range and (c) covers the $3000 - 3030 \text{ cm}^{-1}$ range, highlighting the ν_4 and ν_3 CH_4 bands respectively. The blue COSPAR spectra contain no CH_4 and the overlaid red COSPAR spectra contain 10 ppb CH_4 .

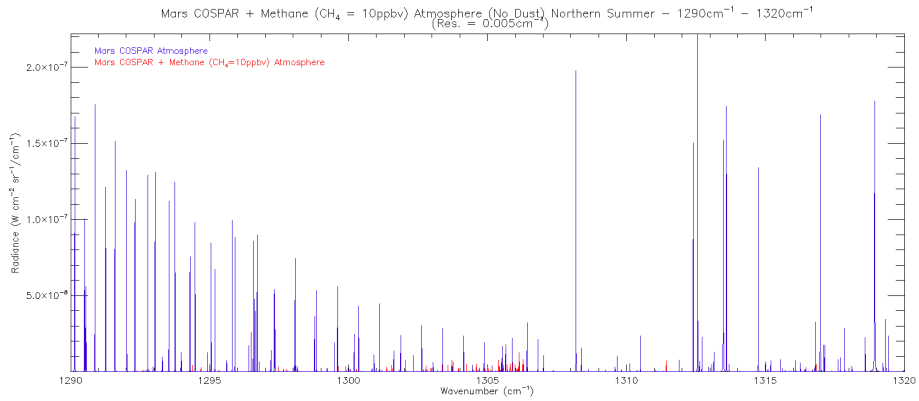


Figure 4.4: A RADTRANS spectrum producing using the COSPAR Mars profile, with and without CH_4 . Calculations were performed in the nadir between $1290 - 1320 \text{ cm}^{-1}$ at a resolution of 0.005 cm^{-1} . The CH_4 features are highlighted from the background COSPAR spectrum in red.

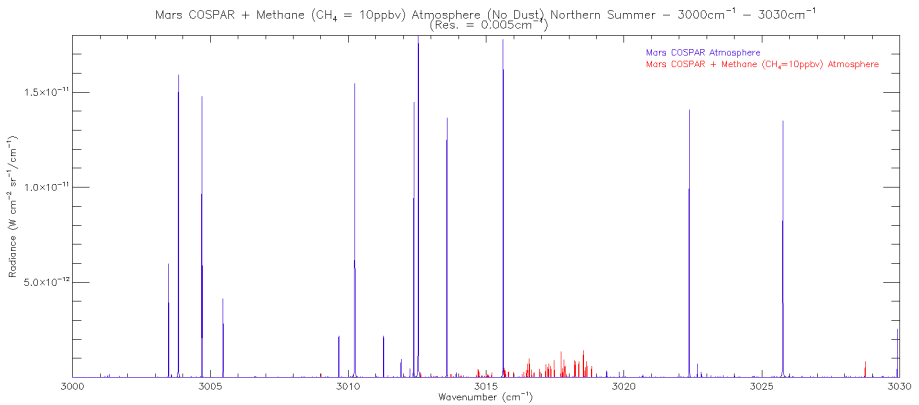


Figure 4.5: A RADTRANS spectrum producing using the COSPAR Mars profile, with and without CH_4 . Calculations were performed in the nadir between $3000 - 3030 \text{ cm}^{-1}$ at a resolution of 0.005 cm^{-1} . The CH_4 features are highlighted from the background COSPAR spectrum in red.

In order to better measure the methane radiance, the CH_4 needs to be extracted from the rest of the Martian COSPAR spectrum. This is done by performing the RADTRANS calculations on the COSPAR atmosphere with and without the CH_4 , then using IDL to plot the difference between the two. This results in a plot containing only CH_4 . The extracted CH_4 for the ν_4 and ν_3 regions are shown in figures 4.6 and 4.7 respectively.

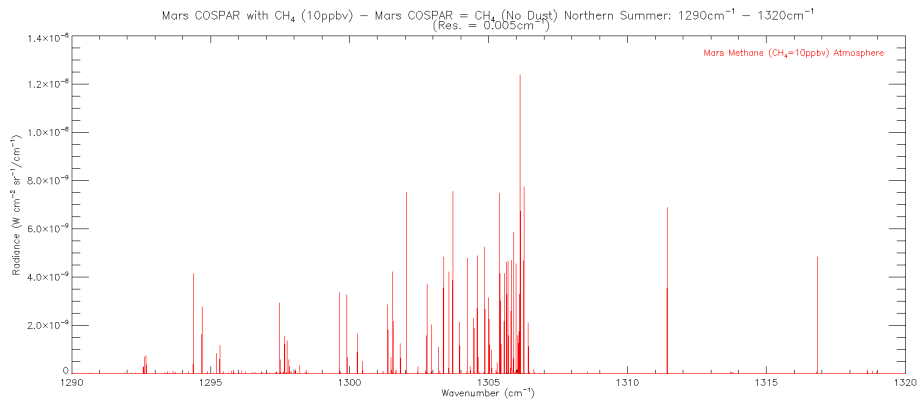


Figure 4.6: CH_4 spectrum between $1290 - 1320 \text{ cm}^{-1}$, at a resolution of 0.005 cm^{-1} . The CH_4 radiance is calculated from the difference of the RADTRANS Mars COSPAR atmosphere spectra with and without CH_4 (10 ppb).

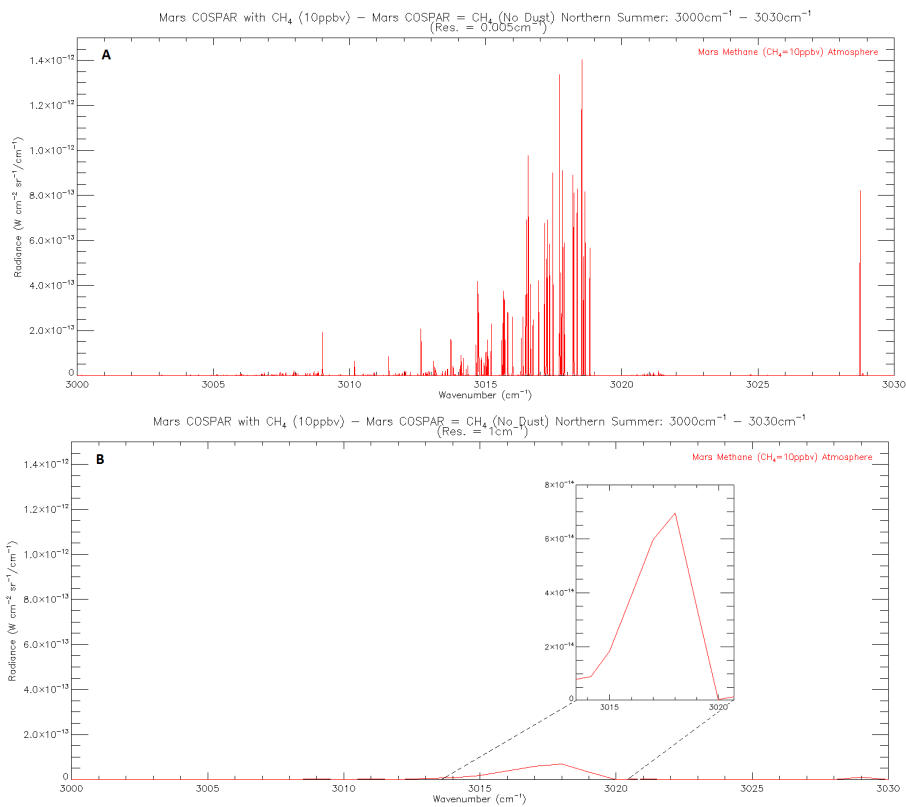


Figure 4.7: CH_4 spectrum between $3000 - 3030 \text{ cm}^{-1}$ (A) at a resolution of 0.005 cm^{-1} and (B) at a resolution of 1 cm^{-1} , plotted at the same scale (An inset window shows a zoom-in on the CH_4 peak). The CH_4 radiance is calculated from the difference of the RADTRANS Mars COSPAR atmosphere spectra with and without CH_4 (10 ppb).

As expected, at a lower resolution, the observed CH_4 radiance decreases. From a resolution of 0.005 cm^{-1} to 1 cm^{-1} the maximum CH_4 peak decreases by approximately a factor of 20. To understand how much the CH_4 radiance decreases with resolution, spectra need to be calculated at a wider range of resolutions. The conventional solution to this would be to run RADTRANS many times using the same atmospheric profile, but each time decrease the resolution by a set interval. This however would require much computing time. Instead, RADTRANS was run only twice for each set of atmospheric variables, once with, and once without 10 ppb CH_4 , at a resolution of 0.005 cm^{-1} . Then using IDL, the radiance values were averaged and re-gridded to a new, user defined, lower resolution. This allowed the Martian atmospheric spectrum, and CH_4 radiances, to be observed at many resolutions in a short amount of time.

Formisano et al. 2004 concentrated on the ν_3 fundamental band (centred at 3019 cm^{-1}) as the signal to noise of the Planetary Fourier Spectrometer (PFS) on Mars Express is much greater in the region around 3000 cm^{-1} . Therefore it was decided to make the ν_3 band the focus of investigation, with less emphasis placed on the ν_4 band. As a result, much of the work that follows was performed between $3000 - 3030 \text{ cm}^{-1}$.

Once the CH_4 radiances were extracted from the background Martian spectra, the peak CH_4 radiance, occurring at 3018 cm^{-1} for the ν_3 band, was determined at each spectral resolution. These peak CH_4 values were then plotted against their corresponding resolutions (figure 4.8). This was done from a resolution of 0.005 cm^{-1} to 1.5 cm^{-1} , at intervals of 0.005 cm^{-1} . It shows that the CH_4 radiance drops off quickly with decreasing resolution. This plot is useful in determining the required minimum resolution of an instrument in order to convincingly detect methane on Mars. This determination will be made later in this chapter once the model has been improved to include Martian dust scenarios, and seasonal atmospheric changes.

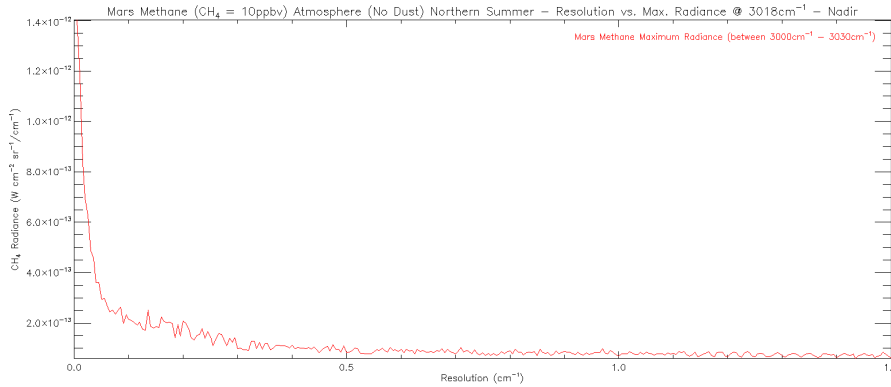


Figure 4.8: Plot of maximum CH_4 radiances, at 3018 cm^{-1} , against their corresponding spectral resolutions for a COSPAR Martian atmosphere. RADTRANS calculations performed from a nadir viewing geometry.

Looking in the Limb

As well as a nadir viewing geometry, RADTRANS was set up to look at the COSPAR Mars atmosphere from a limb viewing angle. The atmosphere was viewed at an angle of 90° and at a height of 0.01 km to the surface. This limb height was chosen in order to calculate the maximum possible radiance from an observation through the atmosphere. A high resolution (0.005 cm^{-1}) RADTRANS calculation was performed on the ν_3 CH_4 region (Figure 4.9A). This was then lowered in resolution to 1 cm^{-1} using IDL (Figure 4.9B). Finally, the CH_4 radiances were extracted from the background COSPAR Mars atmosphere, and the peak CH_4 radiances at resolutions from 0.005 cm^{-1} to 1.5 cm^{-1} , at intervals of 0.005 cm^{-1} , were plotted (figure 4.10). These results show that greater radiances are achieved, by a factor of approximately 2 for the background emission lines, and by a factor of approximately 20 for the methane lines, when looking at an atmosphere in the limb. As a result, the limb is a better choice when remote sensing from planetary orbiting probes.

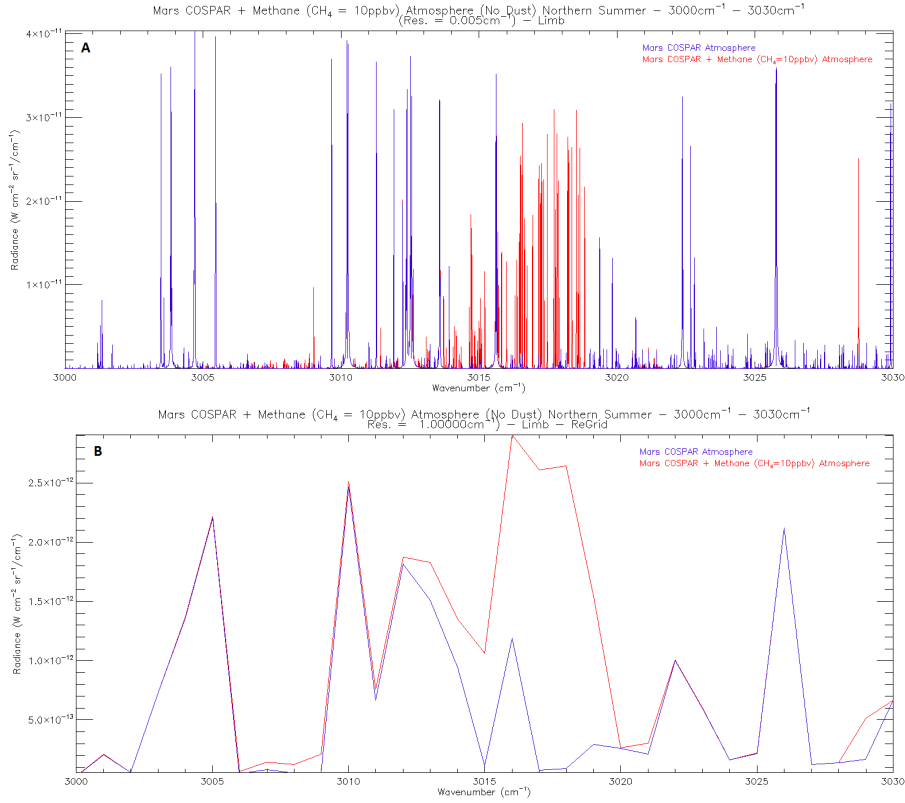


Figure 4.9: Spectra produced using RADTRANS with the COSPAR Mars profile, with and without CH_4 . Calculations were performed in the limb at a tangent height of 0.01 km, between $3000 - 3030 \text{ cm}^{-1}$. (A) is calculated at a resolution of 0.005 cm^{-1} and (B) at a resolution of 1 cm^{-1} . The CH_4 features are highlighted from the background COSPAR spectrum in red.

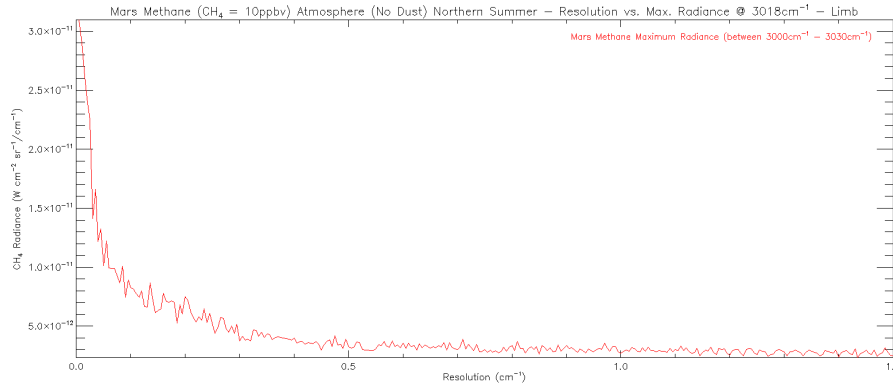


Figure 4.10: *Plot of maximum CH_4 radiances, at 3018 cm^{-1} , against their corresponding spectral resolutions for a COSPAR Martian atmosphere. RADTRANS calculations performed from a limb viewing geometry of tangent height 0.01 km .*

4.3.2 The Mars Climate Database

In order to improve the Martian atmospheric simulations, by providing a range of seasonal atmospheric conditions for the RADTRANS simulations, profiles from the Mars Climate Database [Lewis et al., 1999] were used to reproduce better spectra. The Mars Climate Database (MCD) contains information describing the climate and environment of the Martian atmosphere. It is constructed from General Circulation Model (GCM) numerical simulations developed by Laboratoire de Météorologie Dynamique du CNRS, France in collaboration with the University of Oxford, UK, the Instituto de Astrofísica de Andalucía, Spain, SA, France with support from the European Space Agency (ESA) and Centre National d’Etudes Spatiales (CNES). The Mars GCMs have been extensively validated using available observational data. The MCD contains simulated data for the planet stored on a $5.675^\circ \times 3.75^\circ$ longitude-latitude grid from the surface up to an approximate altitude of 250 km , over all seasons of Mars Year 24 (MY24). This includes information on atmospheric temperature, pressure, radiative fluxes and volume mixing ratios of gases. The Mars Year calendar started on April 11th, 1955 at Martian solar longitude $L_s = 0^\circ$ [Clancy et al., 2000].

MCD data from the northern hemisphere was used so comparisons could be made with the COSPAR produced spectra. Atmospheric profiles were obtained for the MY24 dust and averaging solar flux scenario at coordinates of 48.8°N , 0°E , for month 4 ($L_s = 90^\circ - 120^\circ$), Mars’ summer, and for month 10 ($L_s = 300^\circ - 330^\circ$), Mars’ winter. These months were chosen in order to investigate how seasonal variations in water vapour affect our ability to detect methane. Figure 2.1 shows the variation in atmospheric temperature with altitude in summer and winter. At latitude 48.8°N there is a surface temperature difference of approximately 70 K between midsummer and midwinter. However, atmospheric pressure shows little seasonal difference. Pressure at the surface is between 7 and 9 mbar , and decreases exponentially with altitude, eventually reaching al-

most 0 mbar at 50 km. Figure 4.11 (A) & (B) are vertical profile concentrations of CO₂ (A) and water vapour (B) in the Martian atmosphere, for summer and winter. There is a large difference in low altitude water vapour concentration between the two seasons. This is a result of the surface water ice melting and evaporating during the warmer summer, which increases the volume mixing ratio of water vapour in the atmosphere. In the winter the water vapour condenses out to form ground ice again, therefore only low levels are detected. However, at around 20 km from the surface, the atmosphere is warm enough in winter to still contain a small concentration of H₂O.

The Mars Climate Database profiles the Martian atmosphere from the surface to an altitude of 230 km. The profiles used in this report contain information on the following gases: CO₂, CO, N₂ and H₂O. Like the COSPAR atmosphere, 10 ppb of CH₄ was added to the MCD profiles. RADTRANS calculations were performed in the nadir, and also in the limb at tangent heights of 0.01 km and 22 km, for both the summer and winter.

The results for the MCD summer atmospheres are very similar to that of the COSPAR spectra. The spectral lines for both the nadir and limb viewing geometries were almost identical to their COSPAR counterparts. This is to be expected as the data is based on the same region of the planet, and also at the same time of year as each other. There are however differences in the line strengths. In the nadir, the CH₄ radiances are approximately 50% greater for the MCD spectra. In the limb, at an angle of 90° and at a distance of 0.01 km from the surface, the CH₄ radiances were twice as strong in the MCD spectra as the COSPAR spectra. There are a few reasons that account for the discrepancy in the results between databases: Firstly, the information used in the databases were constructed from different Mars Years, so conditions are slightly different. The MCD profile uses a value of 395 ppm of water vapour at the surface, whereas the COSPAR profile uses 300 ppm. Also, the MCD profile has a greater pressure at the surface of Mars than the COSPAR data. Another explanation is that the top of the atmosphere is set at 100 km in the COSPAR profile, and 230 km for the MCD data. The path length is greater for the MCD atmosphere and as a result an increase in radiance is observed in the spectra.

Figure 4.12 shows MCD spectra produced using RADTRANS, from 3000 – 3030 cm⁻¹, in the nadir for MY24 month 10, i.e. winter. Figure A is a high resolution spectrum (0.005 cm⁻¹), and figure B is a low resolution spectrum (1 cm⁻¹). The results show the same trend as the COSPAR spectra, that at lower resolutions the observed CH₄ radiance decreases. The peak CH₄ radiance decreases by a factor of approximately 20, the same factor that was observed for both the COSPAR and MCD northern hemisphere summer spectra. As before, the CH₄ radiances were extracted from the background MCD atmosphere, and the peak CH₄ radiances were plotted at resolutions from 0.005 cm⁻¹ to 1.5 cm⁻¹, at intervals of 0.005 cm⁻¹ (figure 4.12C). The familiar exponential trend is again evident, but the radiances are approximately a factor of 10 weaker. MCD spectra were also calculated at a limb tangent height of 22 km from the surface. They resulted in radiances that were between 10¹ and 10² weaker than at a limb tangent height of 0.01 km, due to the decrease in atmospheric path length.

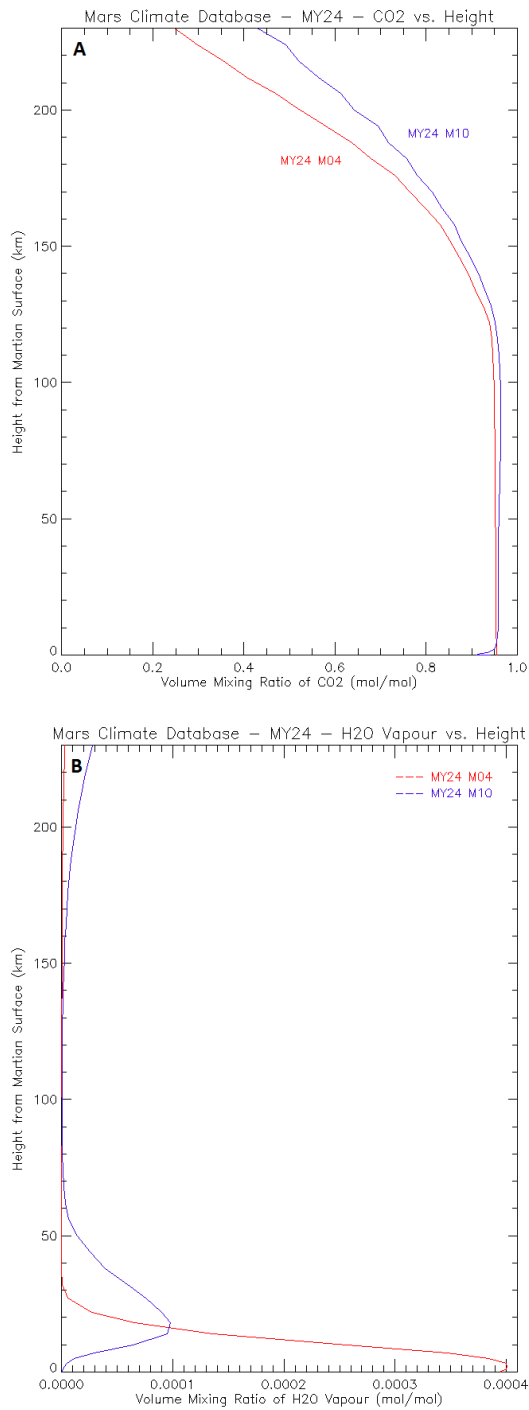


Figure 4.11: Plots showing the volume mixing ratios of two gases, with respect to altitude, in the Martian atmosphere. (A) shows the vertical profile of CO₂ atmospheric concentration, and (B) shows the H₂O concentration. The data were obtained from the Mars Climate Database for the northern hemisphere (at coordinates 48.8°N, 0°E). The red profile represents a Martian summer and blue a Martian winter.

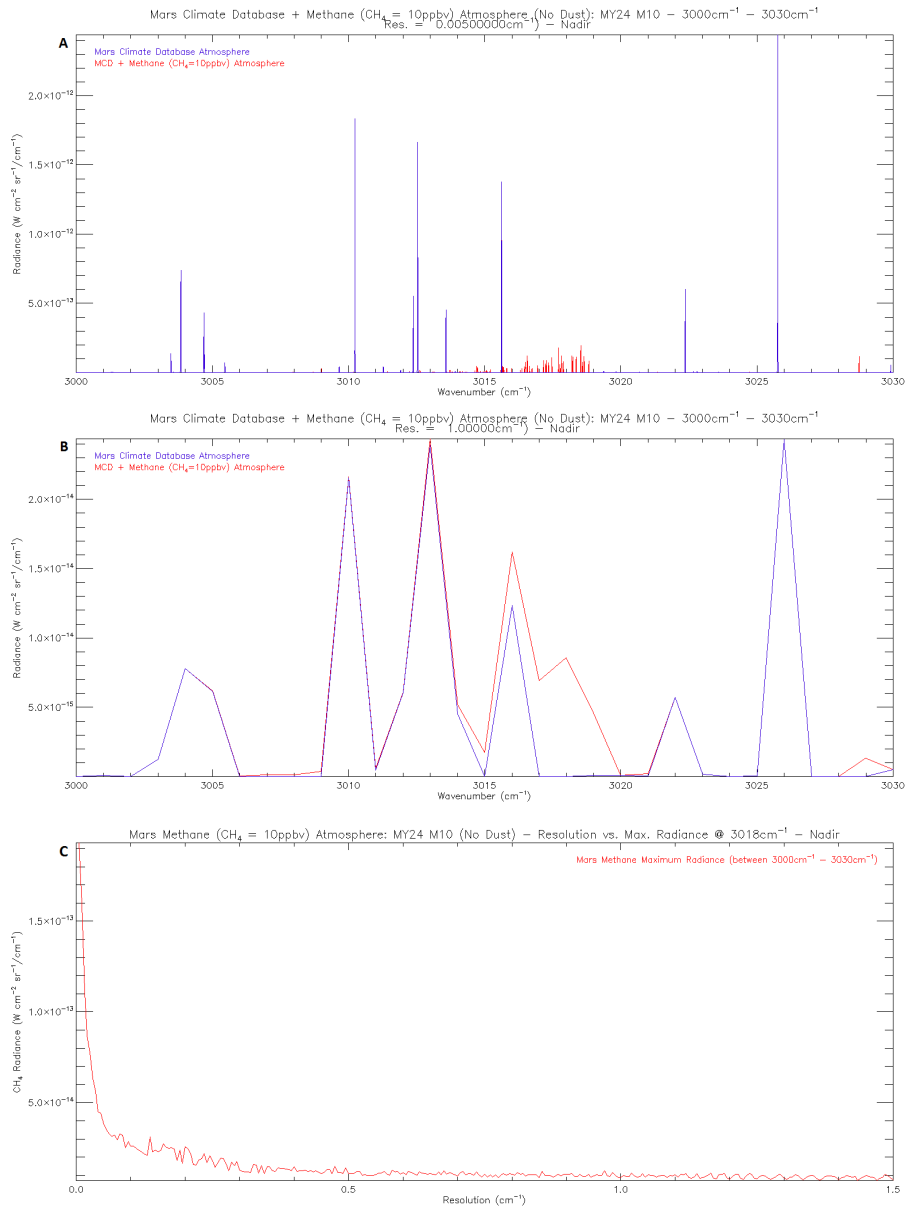


Figure 4.12: *High Resolution RADTRANS Mars Climate Database spectra, containing CO₂, CO, N₂ & H₂O, for the northern hemisphere (at coordinates 48.8°N, 0°E) during the winter of Mars Year 24. The spectra are calculated in the nadir at an altitude of 230 km, covering the spectral range from 3000 – 3030 cm⁻¹. (A) is calculated at a resolution of 0.005 cm⁻¹ and (B) at a resolution of 1 cm⁻¹. The CH₄ features (red) are highlighted from the background MCD spectrum (blue). (C) is a plot of the maximum CH₄ radiance against spectral resolution of RADTRANS MCD spectra. The peak CH₄ value, at the centre of the ν₃ band (~ 3018 cm⁻¹), is calculated and plotted at resolutions from 0.005 cm⁻¹ to 1.5 cm⁻¹ at intervals of 0.005 cm⁻¹.*

4.3.3 Adding Dust to the Model

Dust in the Martian atmosphere can severely affect spectral measurements. The more extreme the dust storm, the more difficult it becomes to distinguish individual features in the spectrum. Planet wide dust storms occur every few years and have been witnessed by Mariner 9 and Mars Global Surveyor. It is therefore important to consider dust scenarios when undertaking atmospheric modelling. The dust models used in RADTRANS are now discussed.

As well as the .prf file that defines the atmospheric profile, another .prf file is required that contains information about the dust concentration in the atmosphere. This file is created using the RADTRANS program ‘Dust_profile’. In order to generate the dust profile the program must read in the corresponding atmospheric profile, in this case, cospar.prf. A steady state dust model was selected, where the dust is constant at low altitudes, and then falls off at a defined rate; this is determined by the inflection coefficient.

Figure 4.13 shows a vertical dust profile of the Martian atmosphere. It assumes steady state conditions and a constant vertical diffusivity, K . ν is defined as the ratio of the characteristic aerosol diffusion to the gravitational settling time at the planetary surface. Steady state dust distributions are calculated using the aerosol mixing ratio, $q(z)$:

$$q(z) = q_0 \exp \left\{ \nu \left[1 - \exp \left(\frac{z}{H} \right) \right] \right\}$$

where q_0 is the value of the specific dust concentration, q , at $z = 0$, and $\nu = H \omega_0^* / K$, where ω_0^* is the terminal velocity of the dust particles and H is the pressure scale height. As the mixing is increased, the diffusion time, t_D , and ν become smaller, and the dust extends to greater heights. A uniform mixing condition, where $\nu = 0$, would be represented by a vertical line on the plot. The top of the dust layer, Z_t , is defined as $Z_t = -H \ln \nu$. This is the level at which the settling time $t_s(z)$ becomes equal to the diffusion time t_D . Images sent back from Mariner 9 during its limb observation of a Martian dust storm indicated dust up to at least 50 km [Leovy et al., 1972]. A value of $Z_t \approx 50$ km corresponds to $\nu = 0.007$, and is plotted in figure 4.13. This value is used as the inflection coefficient in the ‘Dust_profile’ program.

Information regarding particle scattering is stored in an .xsc file. This is created by the program ‘Makephase’, which calculates phase functions of spherical particles according to Mie theory. The Mie scattering, log-normal distribution was used to calculate the spectra in this report. The dust has the following size distribution:

$$n(r) = \frac{1}{r} \exp \left[-\frac{(\ln r - \ln r_g)^2}{2\sigma_g^2} \right] \quad [\text{RADTRANS Manual}]$$

where r_g is the mean radius of the particle distribution and σ_g is the mean value of $\ln(r)/\ln(r_g)$. The value of r_g was chosen, using data from Wolff and Clancy [2003], based on the dust conditions that were being simulated. For a normal dust scenario, a mean particle radius of 1.6 μm , with a distribution width of 0.3 μm was used. For a maximum dust storm case, a mean particle radius of 3.0 μm , with a distribution width of 0.3 μm was used. The same particle distribution width was used in all dust cases by Wolff et al. [2006] in order evaluate independently the effect of varying dust size. ‘Makephase’ also

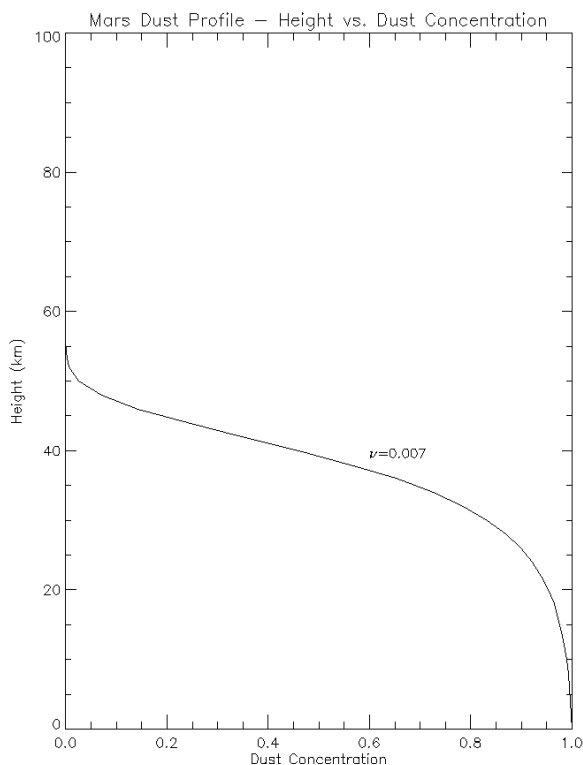


Figure 4.13: *Vertical dust profile for the Martian atmosphere. ν is the ratio of the characteristic diffusion time to the gravitational settling time at the planetary surface. $\nu = 0.007$ corresponds to a maximum dust layer height, Z_t , of approximately 50 km [Conrath, 1975].*

requires the refractive index of the dust. This is read in from a file containing data from Wolff and Clancy [2003] which includes the real and imaginary parts of the refractive index. All input information is used to calculate the extinction cross-section and single scattering albedo of the dust particles, which is then written to the .xsc file.

Finally, the number of dust particles per cm^2 of atmosphere at each vertical layer is required. This is calculated using the ‘aerosol_tau’ program (Teanyby, private communication) and uses the dust concentration values created by the ‘Dust_profile’ program, along with the particle scattering variables in the .xsc file, and the COSPAR atmospheric profile. The dust optical depth was rescaled to a selected optical depth at 1075 cm^{-1} . An optical depth of $\tau = 0.25$ was used for the average dust opacity on Mars, and a value of $\tau = 3.0$ was used for a major dust storm case [Lolachi, 2008].

The dust profiles were incorporated into RADTRANS simulations of the COSPAR atmospheric profiles. Once again simulated spectra were produced at a high resolution of 0.005 cm^{-1} for nadir and limb viewing and the ν_3 and ν_4 fundamental bands were studied.

An Atmosphere Under Normal Dust Conditions

The spectra in figures 4.14 & 4.15 were produced in the nadir under a normal dust scenario. Dust particles of mean radius $1.6 \mu\text{m}$, and distribution width $0.3 \mu\text{m}$, were simulated. An optical depth of $\tau = 0.25$ was used for the average dust opacity of the Martian atmosphere. Figure 4.14 covers the $3000 - 3030 \text{ cm}^{-1}$ spectral range, and figure 4.15 covers the $1290 - 1320 \text{ cm}^{-1}$. Figure (A) in both display a high resolution spectrum (0.005 cm^{-1}), and figure (B) a low resolution spectrum (1 cm^{-1}). (C) are the maximum CH_4 radiances plotted against spectral resolution.

The spectra show that the addition of dust to the COSPAR profile increased the spectral radiance by a factor of about 10^1 . This is due to the scattering of radiation which occurs in the measured direction. However, the background shape now features a slope that decreases with increasing wavenumber. This effect is due to the added dust in the model. It is characteristic of blackbody with low emissivity, with features of the dust superimposed on it.

It can be seen from the spectra that for a normal dust case ($\tau = 0.25$), methane detection is clearly visible at very high resolutions (0.005 cm^{-1}), but becomes more difficult at lower resolutions (e.g. 1 cm^{-1}). The overall CH_4 radiance has decreased, by approximately a half, compared to the model containing no dust. The limb measurements that included dust show a similar development to the nadir case; an overall increase in radiance. The difference is that the limb measurements show a switch to an absorption spectra instead of emission spectra.

A Maximum Dust Storm Scenario

The spectra in figures 4.16 & 4.17 were produced in the nadir for a scenario involving a maximum dust storm. Dust particles of mean radius $3.0 \mu\text{m}$, and distribution width $0.3 \mu\text{m}$, were simulated. An optical depth of $\tau = 3.0$ was used for the average dust opacity during a dust storm in the Martian atmosphere. Figure 4.16 covers the $3000 - 3030 \text{ cm}^{-1}$ spectral range, and figure 4.17 covers the $1290 - 1320 \text{ cm}^{-1}$. Figure (A) in both display a high resolution spectrum (0.005 cm^{-1}), and figure (B) a low resolution spectrum (1 cm^{-1}). (C) are the maximum CH_4 radiances plotted against spectral resolution. The spectra now show a characteristic absorption signature; as the dust levels have increased, the molecules in the atmosphere have switched to absorbing instead of emitting.

In the case of a dust storm, all features of the spectrum have become challenging to identify, especially in the $3000 - 3030 \text{ cm}^{-1}$ spectral range. The results show that as the level of dust increases the ability to detect the methane becomes far more difficult. For the maximum dust storm scenario ($\tau = 3.0$), methane identification at low resolution (1 cm^{-1}) is now almost impossible in the ν_3 band. This result questions the work by Formisano et al. [2004]. They used data from the PFS on Mars Express, which has a spectral resolution of 1.3 cm^{-1} , to calculate a CH_4 amount of $10 \pm 5 \text{ ppb}$, in the ν_3 region. The measurements were made while a major dust storm was in development. A spectrum of their results is shown in figure 3.5.

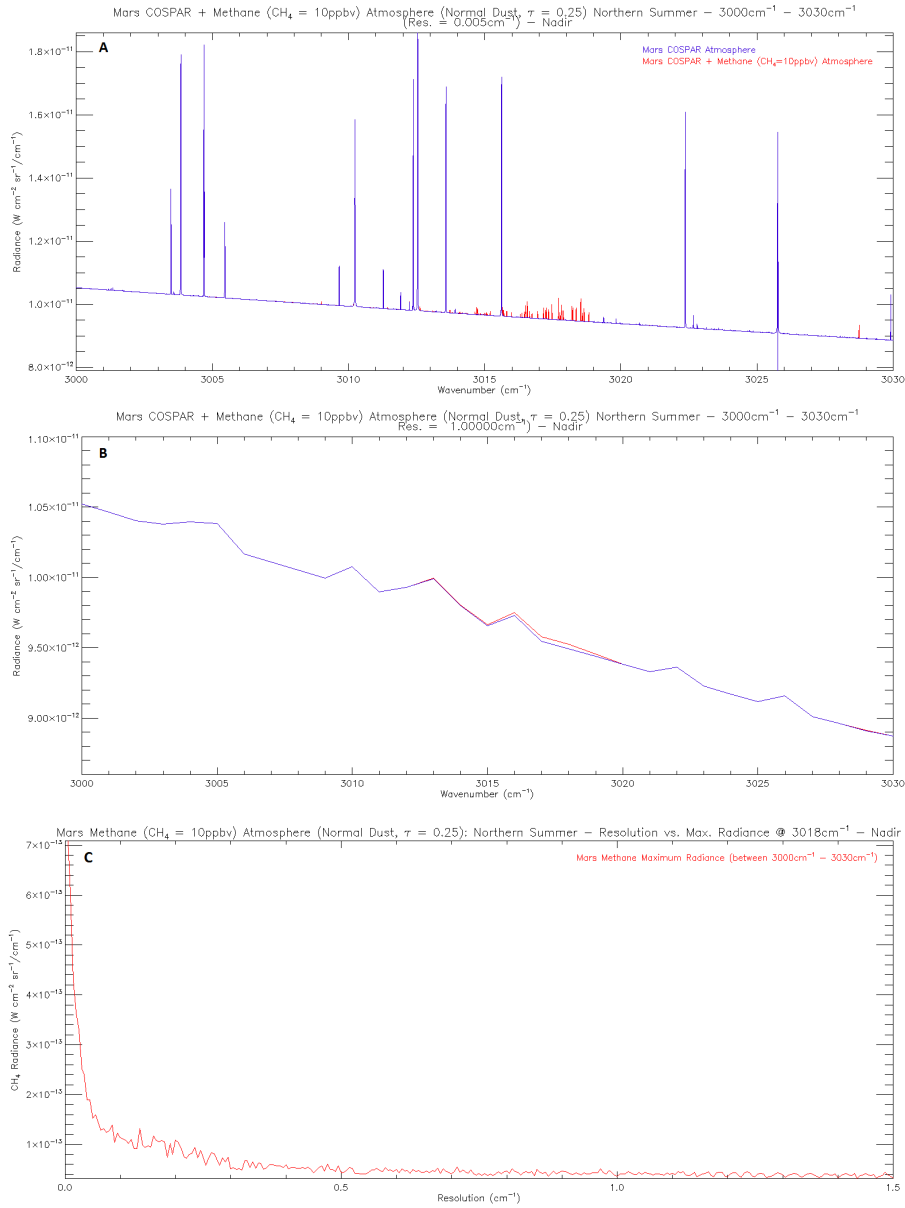


Figure 4.14: Spectra producing using RADTRANS with the COSPAR Mars profile, with and without CH₄, for a normal dust case (mean particle radius = 1.6 μm and $\tau = 0.25$). Calculations were performed in the nadir, between 3000 – 3030 cm^{-1} . (A) is calculated at a resolution of 0.005 cm^{-1} and (B) at a resolution of 1 cm^{-1} . The CH₄ features (red) are highlighted from the background COSPAR spectrum (blue). (C) is a plot of the maximum CH₄ radiance against spectral resolution of RADTRANS COSPAR spectra. The peak CH₄ value, at the centre of the ν_3 band ($\sim 3018 \text{ cm}^{-1}$), is calculated and plotted at resolutions from 0.005 cm^{-1} to 1.5 cm^{-1} at intervals of 0.005 cm^{-1} .

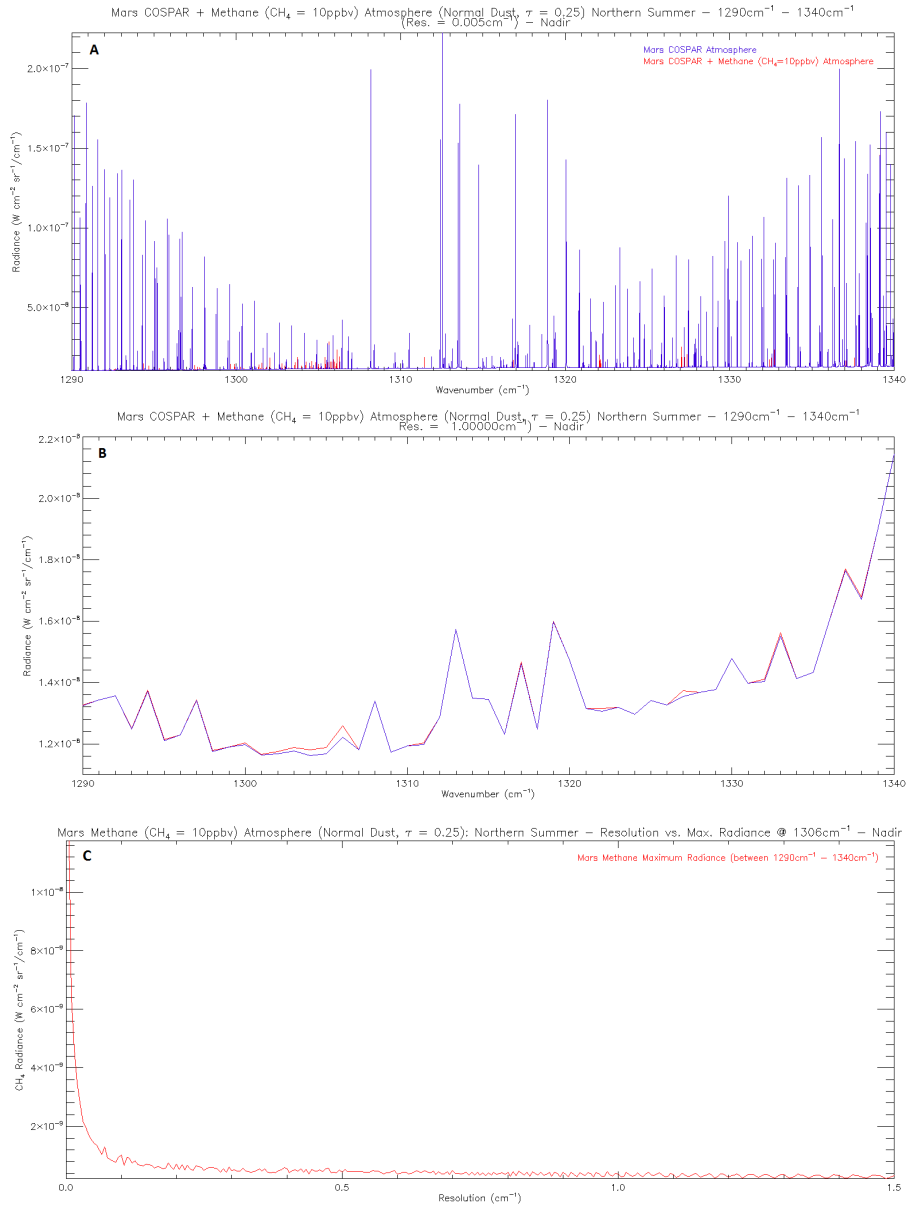


Figure 4.15: Spectra producing using RADTRANS with the COSPAR Mars profile, with and without CH₄, for a normal dust case (mean particle radius = 1.6 μm and $\tau = 0.25$). Calculations were performed in the nadir, between 1290 – 1340 cm^{-1} . (A) is calculated at a resolution of 0.005 cm^{-1} and (B) at a resolution of 1 cm^{-1} . The CH₄ features (red) are highlighted from the background COSPAR spectrum (blue). (C) is a plot of the maximum CH₄ radiance against spectral resolution of RADTRANS COSPAR spectra. The peak CH₄ value, at the centre of the ν_3 band ($\sim 3018 \text{ cm}^{-1}$), is calculated and plotted at resolutions from 0.005 cm^{-1} to 1.5 cm^{-1} at intervals of 0.005 cm^{-1} .

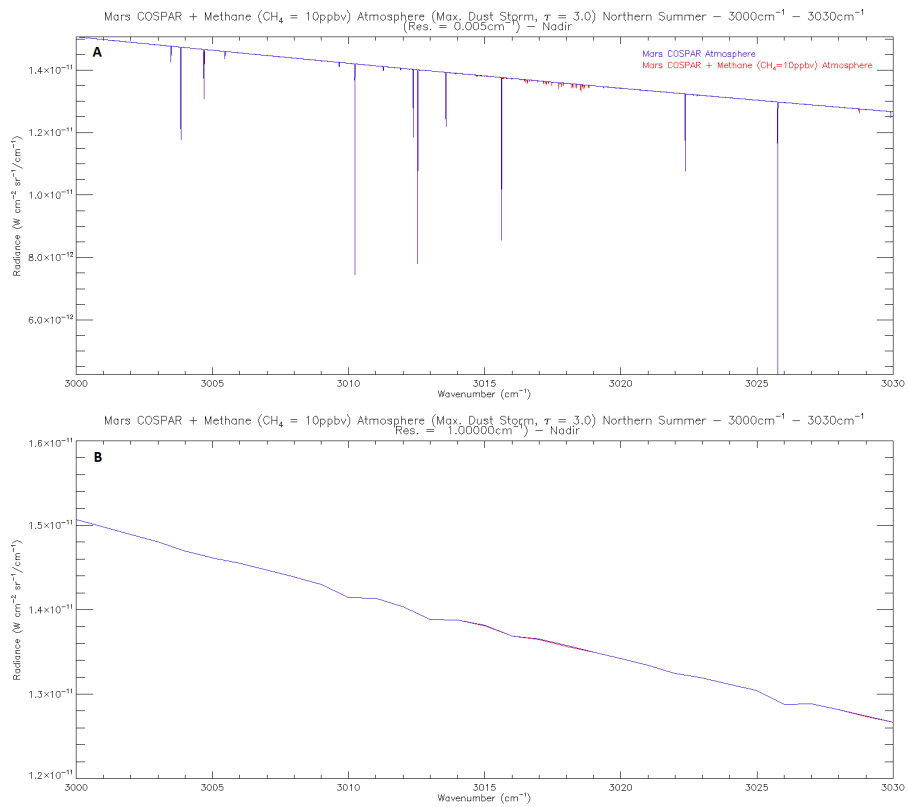


Figure 4.16: Spectra producing using RADTRANS with the COSPAR Mars profile, with and without CH_4 , for a maximum dust storm case (mean particle radius = $3.0\ \mu m$ and $\tau = 3.0$). Calculations were performed in the nadir, between $3000 - 3030\ cm^{-1}$. (A) is calculated at a resolution of $0.005\ cm^{-1}$ and (B) at a resolution of $1\ cm^{-1}$. The CH_4 features (red) are highlighted from the background COSPAR spectrum (blue).

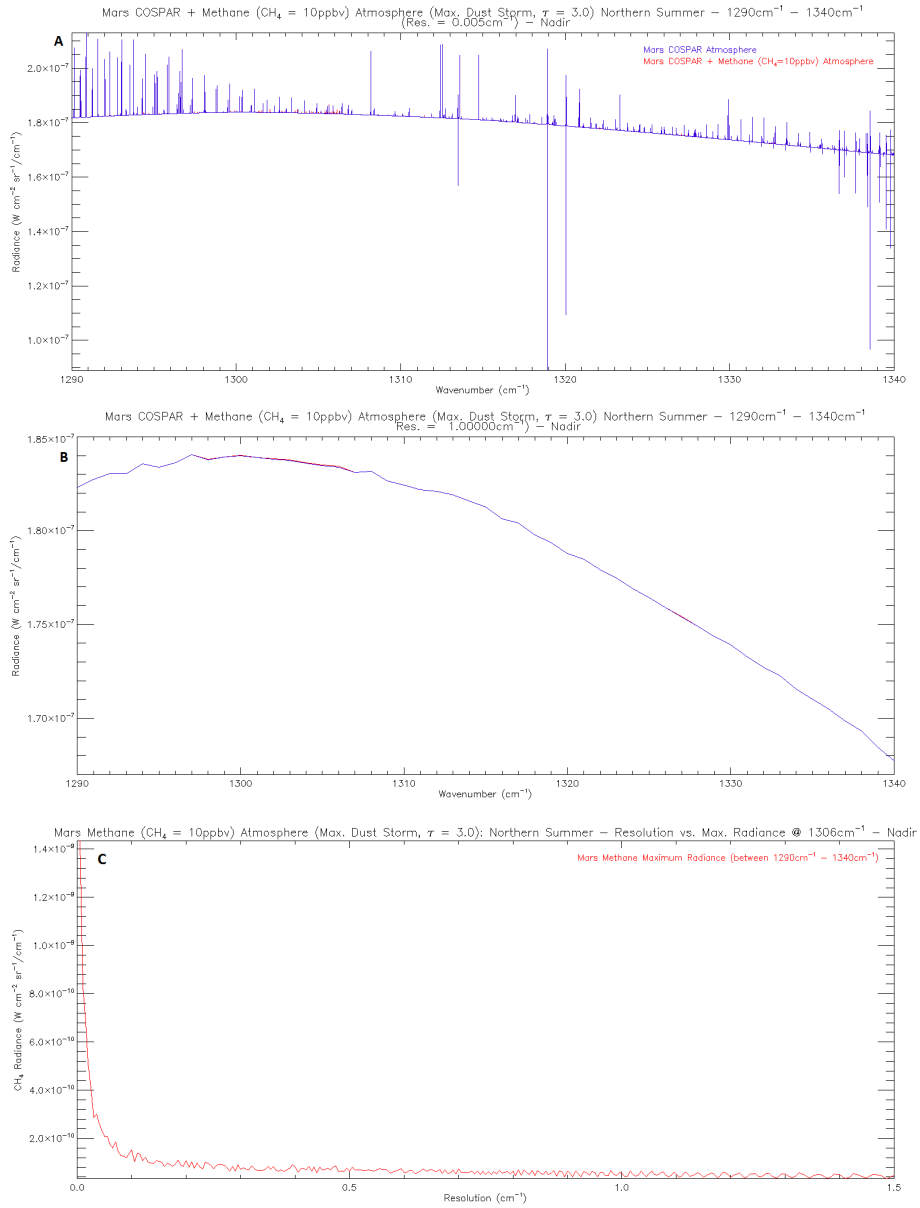


Figure 4.17: Spectra producing using RADTRANS with the COSPAR Mars profile, with and without CH_4 , for a maximum dust storm case (mean particle radius = $3.0 \mu\text{m}$ and $\tau = 3.0$). Calculations were performed in the nadir, between $1290 - 1340 \text{ cm}^{-1}$. (A) is calculated at a resolution of 0.005 cm^{-1} and (B) at a resolution of 1 cm^{-1} . The CH_4 features (red) are highlighted from the background COSPAR spectrum (blue). (C) is a plot of the maximum CH_4 radiance against spectral resolution of RADTRANS COSPAR spectra. The peak CH_4 value, at the centre of the ν_3 band ($\sim 3018 \text{ cm}^{-1}$), is calculated and plotted at resolutions from 0.005 cm^{-1} to 1.5 cm^{-1} at intervals of 0.005 cm^{-1} .

Chapter 5

Laser Heterodyne Radiometry for Remote Sensing of Martian Methane

5.1 Fourier Transform Spectroscopy

Fourier transform spectroscopy is a measurement technique where spectra are collected based on the analysis of the temporal coherence of a radiative source, using time domain measurements of the EM radiation. Fourier transform spectrometers rely on the same principles as a Michelson interferometer. The difference is that after the incident signal is split into two beams, one is reflected off a fixed mirror, while the other is reflected off a moving mirror. The movement of the second mirror causes a change in interference, which results in a time varying signal at the detector. Measurements of the signal are made at discrete positions of the moving mirror, and the spectrum is reconstructed by Fourier transforming the signal at the detector. The major advantage of Fourier transform spectroscopy over a grating spectrometer is the speed at which it operates as it measures all spectral intervals simultaneously [Hanel et al., 2003].

Experiments are undertaken at the Molecular Spectroscopy Facility (MSF) at the Rutherford Appleton Laboratory (RAL). Spectral measurements are made using a Bruker IFS 125HR high resolution Fourier transform IR spectrometer (Figure 5.1). The instrument is based on a Michelson interferometer with a maximum optical path difference of 6 m, providing a resolving power of greater than 10^6 in the mid-IR (spectral resolution = 0.001cm^{-1}) and time resolutions as high as $5\ \mu\text{s}$. The spectrometer can acquire high-quality spectroscopic data over the entire spectral range, starting from the far IR at $5\ \text{cm}^{-1}$ up to the UV range above $50,000\text{cm}^{-1}$. The mass of the spectrometer, including the optics bench and vacuum pump, is 675 kg [Bruker IFS 125HR User Manual, 2006].

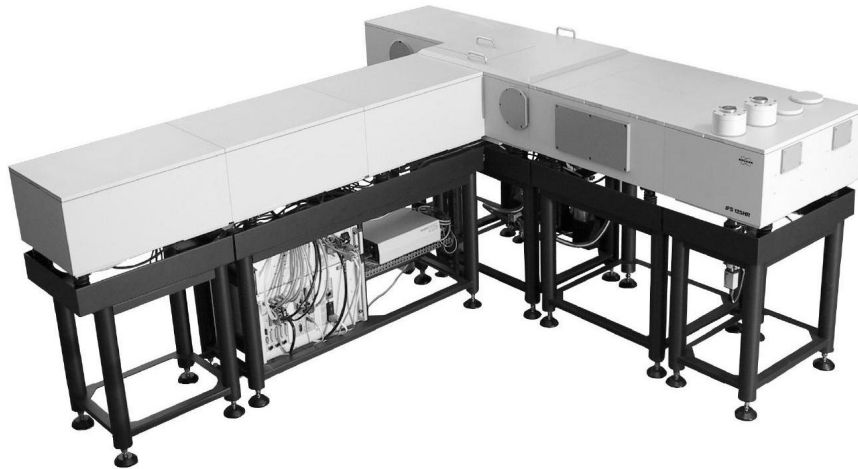


Figure 5.1: *The Bruker IFS 125HR high resolution Fourier Transform IR Spectrometer [Bruker IFS 125HR User Manual, 2006].*

Gas Cell

A gas cell, 30 cm in length with an internal diameter of 34 mm, is used to contain the gases for study. It is made of stainless steel and has KBr windows at either end. It has an internal volume of 272 cm³. The gas cell is mounted inside the evacuated sample compartment of the spectrometer where the spectrometer beam can pass through the windows and the sample inside. The gas cell is cooled by liquid nitrogen, and can be varied in temperature to simulate any Martian altitude.

5.2 Laser Heterodyne Radiometry

Laser heterodyne radiometers (LHRs) have been used extensively, and with much success, for atmospheric studies, such as the work by Weidmann et al. [2007b] on stratospheric ozone, mainly because of their ability to make measurements with an ultrahigh spectral resolution. Notable accomplishments of planetary atmospheric retrievals from IR heterodyne measurements are discussed by Kostiuk and Mumma [1983].

5.2.1 Heterodyne Detection

The heterodyne method down-converts the received signal to a lower, intermediate frequency (IF) signal, in order to process it more easily. This is done by mixing the incident radiation with that from the local oscillator (LO) at the detector with a nonlinear response (see Menzies [1976] and Teich [1985] for more details). The IF signal is divided and amplified without degradation of the signal-to-noise ratio (SNR), which allows efficient spectral multiplexing [Weidmann et al., 2007a]. The advantages of IR laser heterodyne spectroscopy are discussed.

5.2.2 Instrument Sensitivity

The noise equivalent power (NEP) for an ideal heterodyne radiometer is given by the following equation:

$$NEP = \frac{h\nu}{\eta} \sqrt{\frac{B}{\tau}} \quad [1]$$

where η is the heterodyne efficiency, h is the Planck constant, ν is the frequency, B is the receiver bandwidth, and τ is the integration time.

5.2.3 Comparing the LHR with a Fourier Transform Spectrometer

Current high-resolution IR instruments are typically based on Fourier transform spectrometers. These instruments require large optical path differences to achieve a high spectral resolution, which result in their large physical size and mass (see section 5.1). The design of the LHR allows for a compact and lightweight (approx. 10 – 15 kg) instrument. The current quantum cascade laser-based LHR at the MSF has a dimension of 0.75 m x 0.75 m and there is potential for miniaturization through optical integration. [Weidmann et al., 2007b] also demonstrate that a carefully selected specific high resolution microwindow provides as much information as a medium resolution radiometer covering a broad spectral range. This additional feature is another advantage that favours the development of the LHR instrument over current Fourier transform spectrometers.

When performing surveys of planetary atmospheres, a Fourier transform spectrometer is an ideal instrument. It can look over a wide spectral range in order to identify many constituents in the atmosphere. But to target a particular molecule, such as methane, then a more specialised instrument, such as the LHR, is required. The equation for the SNR of a FTS is:

$$SNR_{FTS} = I(\nu, T) U \xi \Delta\nu D^* \sqrt{\tau(A_D)^{\frac{1}{2}}} \quad [2]$$

where $I(\nu, T)$ is the Planck equation, U is the FTS throughput, ξ is the efficiency, $\Delta\nu$ is the resolution, D^* is the detectivity, and A_D is the physical area of the detector element. Comparing the SNR of the FTS to the SNR of the LHR we get:

$$\frac{SNR_{HET}}{SNR_{FTS}} = \frac{c^2 \sqrt{A_D}}{2h U \xi D^*} \eta \frac{1}{\nu^3 \sqrt{\Delta\nu}} \quad [3]$$

The first term is a constant, the second term is related to the performance of the FTS, and the last term shows that heterodyne radiometry is more favourable at higher resolutions. Figure 5.2 illustrates this as plot of the signal-to-noise ratio of the LHR vs. a FTS. The graph was generated for a shot-noise limited heterodyne radiometer operating at 3.3 μm (3030 cm^{-1}) and 7.7 μm (1300 cm^{-1}), with a 50% photomixer heterodyne efficiency. The following values are used to produce the graph, as they represent specifications for a typical commercial FTS: $A_D = 1 \text{ mm}^2$, $U = 0.01 \text{ cm}^2 \text{ sr}$, $\xi = 0.1$, and $D^* = 8 \times 10^{10} \text{ cm}\sqrt{\text{Hz}} \text{ W}^{-1}$. The graph shows that a laser heterodyne radiometer operating in the 7.7 μm region of the spectrum performs better than a FTS at resolutions greater

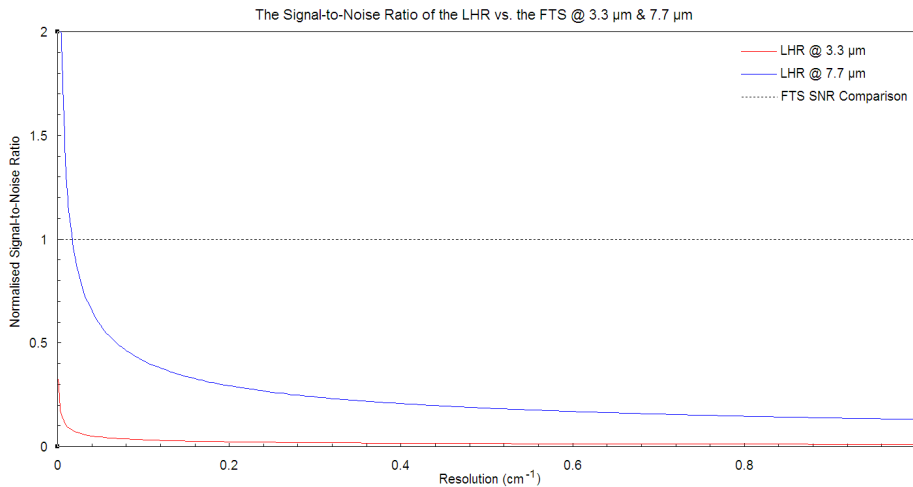


Figure 5.2: A plot of the normalised signal-to-noise ratio of the LHR compared to a FTS. An ideal heterodyne radiometer operating at $3.3 \mu\text{m}$ is shown in red, and at $7.7 \mu\text{m}$ in blue, both with a 50% photomixer heterodyne efficiency. The SNR of a FTS is represented by the black dotted line.

than 0.02 cm^{-1} . However, in the $3.3 \mu\text{m}$ spectral region, a Fourier transform spectrometer outperforms the LHR. The spectral coverage of the FTS is around 500 times wider than the LHR, but the resolution of the LHR is superior to that attainable by most FTS instruments.

Figure 5.3 shows a plot of maximum CH_4 radiances against spectral resolution, producing using RADTRANS with data from the COSPAR atmospheric Martian profile for northern summer. The spectral resolution of the LHR, MIPAS on the ENVISAT satellite, and PFS on Mars Express are compared against the simulated methane radiances. It shows that the LHR has the greatest spectral resolution (0.005 cm^{-1}) followed by MIPAS (0.035 cm^{-1}) and finally the PFS onboard Mars Express (1.3 cm^{-1}).

5.3 Quantum Cascade Laser LHRs

The majority of previous spectroscopy studies using the IR heterodyne technique have been carried out with a CO_2 gas laser as the LO source (e.g. Fast et al. [2006a,b]). However, the invention of mid-infrared quantum cascade lasers (QCLs) [Faist et al., 1994], have offered a new alternative. QCLs offer the prospect of room temperature operation coupled with a wide spectral tuning range. They also have the advantage of being extremely compact, robust and reliable devices which make them ideal candidates for flight and satellite deployment. Quantum cascade lasers differ in a fundamental way to normal semiconductor lasers. Electrons cascade down a potential staircase successively emitting photons at each step. These steps consist of coupled quantum wells in which population inversion between the discrete excited states of the conduction band is achieved via tunnelling control [Faist et al., 1994]. This is unlike diode lasers which emit only one photon over the same cycle. This means that QCLs have

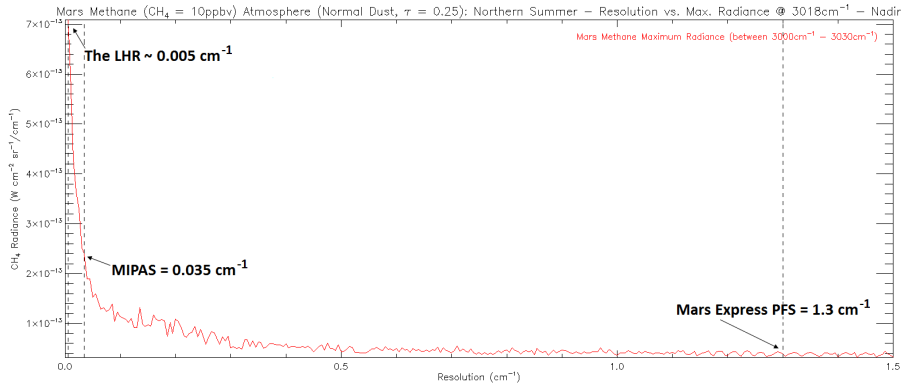


Figure 5.3: Plot of the maximum CH_4 radiances against spectral resolution for a COSPAR northern summer Martian atmosphere during normal dust conditions ($\tau = 0.25$). The peak CH_4 value, at the centre of the ν_3 band ($\sim 3018 \text{ cm}^{-1}$), is calculated and plotted at resolutions from 0.005 cm^{-1} to 1.5 cm^{-1} at intervals of 0.005 cm^{-1} . RADTRANS calculations performed from a nadir viewing geometry. The dashed lines represent the spectral resolution of three instruments: (from left to right) The LHR at the MSF, MIPAS on the ENVISAT satellite, and PFS on Mars Express.

the ability to outperform diode lasers operating at the same wavelength. A major feature of QCLs, which has been exploited for absorption spectroscopy, is their ability to be continuously tuned in frequency. The LHR uses this to sweep the frequency of the LO, and perform the analysis. This method avoids the need for any IF signal analysis. The spectral coverage of a heterodyne receiver is determined by the LO frequency, the bandwidth of the photomixer and the related electronics [Weidmann et al., 2007a].

A schematic of the QCL LHR optical layout is shown in figure 5.4.

5.4 Simulating Mars in the Laboratory

The work on the LHR is undertaken at the Molecular Spectroscopy Facility (MSF) at the Rutherford Appleton Laboratory (RAL). The instrument will first be tested to determine its ability to measure methane gas transmission through small gas cells. A Martian atmosphere will then be replicated which will include aerosols that represent typical dust concentrations. These will range from average dust conditions to the levels seen during a major dust storm. Data from the LHR will be processed and wavelength calibrated transmission spectra will be produced. The instruments sensitivity and discrimination of overlapping spectral features will be analysed. Also, a side-by-side spectroscopic comparison will be made between the LHR and a high resolution Fourier transform spectrometer (the Bruker IFS 125HR). A conclusion will be made whether methane can be detected using the LHR as well, or better, than the FTS. If successful, consideration will then be made for developing the instrument further in order to make remote sensing measurements of the Martian atmosphere. The instruments potential for a future Martian orbiter will also be assessed.

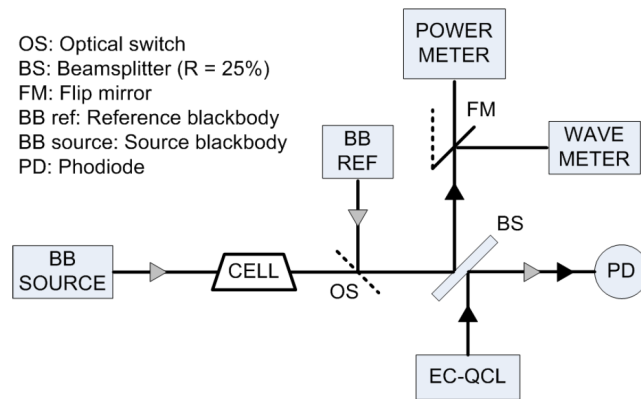


Figure 5.4: Schematic optical layout of the external cavity quantum cascade laser heterodyne spectro-radiometer [Weidmann and Wysocki, 2008].

Chapter 6

Conclusions

The main focus on the research so far has been built around the previous work into the search for methane on Mars. This has been done through simulations of the Martian atmosphere using RADTRANS to identify methane characteristics in the background spectra. Krasnopolsky et al. [2004] and Formisano et al. [2004] both concluded a CH₄ mixing ratio of 10 ppb, and this value was used during calculations.

The results from the RADTRANS simulations in this report show how challenging methane on Mars is to detect, particularly due to the dust and water vapour in the atmosphere that obstruct measurements. Water vapour has strong spectral features around the same areas as the fundamental methane bands, especially the CH₄ ν_4 band at 3.3 μm . H₂O contaminates the methane signal, and makes methane detection difficult, particularly at low resolutions. Dust also has an influence on the observed spectrum and therefore different dust scenarios were calculated. The conclusion is that with the added dust, the overall radiance increases, due to scattering in the measured direction, but the ability to distinguish individual features become more difficult. This was especially true in the case where a maximum dust storm was replicated. Methane could no longer be detected. For a normal dust case however, methane discrimination is possible, but as expected, at low resolutions this again become more difficult. In order to make a clear identification, higher resolutions and longer integration times are required.

The results conclude that the spectral resolution of the instrument is a critical factor in studies. The lower the instrument resolution the more difficult detection becomes. Therefore a higher resolution instrument is necessary to make more conclusive determinations. The results show that a resolution approximately greater than 0.3 cm^{-1} is required to make a conclusive CH₄ detection. An instrument like the LHR can provide that required superior spectral resolution, with the many advantages it brings over conventional spectrometers. The next stage of this research will look at that instrument in more detail and work to adapt it for remote sensing of the Martian atmosphere.

Chapter 7

Future Work

A timeline of future work is detailed below:

September - October 2009

- Perform tests on the hollow waveguide at the MSF at RAL. This technology should help miniaturise the LHR and make it more robust. It is being developed in collaboration with QinetiQ.
- Gain familiarity with the aerosol chamber and test a range of silicates. Select the right aerosol that best represents the Martian atmospheric dust.

November 2009 - January 2010

- Design the experiment to study methane in the laboratory.
- Construct a Mars-like atmosphere in a gas cell, containing the correct concentration of gases, along with the 10 ppb of CH₄.
- Perform measurements on the cell with the IFS 66V spectrometer at AOPP and also at the MSF.
- Add the aerosol to simulate Martian dust conditions and calculate the spectrum of this 'Martian' environment.

February - March 2010

- Test the noise levels of the LHR instrument and setup.

April - May 2010

- Take the knowledge gained at the MSF and use it to build a more comprehensive simulated Martian atmosphere in RADTRANS:
- Already looked at 2 dust cases: A normal Martian atmosphere (dust of mean radius 1.6 μm) and a Martian atmosphere experiencing a major dust storm (the mean radius of dust particles is taken to be 3.0 μm). Simulate different size dust particles and concentrations to see the effect on the methane detection; resulting a better dust model.
- Use information from the Mars Climate Database to investigate different latitudes to see how the Martian atmosphere varies across the planet. Current work

has so far focused on the Northern Hemisphere. Study lower latitudes including the Martian equator and the Southern Hemisphere.

- Vary the concentrations of water vapour and determine how this effects methane detection. Correlate with the differences in seasonal water vapour and determine the best time of year to measure the methane; when there is the least water vapour in the atmosphere to interfere with detection.
- Determine the best satellite instrument viewing geometry for studying the Martian atmosphere to see which gives the greatest radiances. Evaluate different limb tangents and simulate atmospheric scans for a solar occultation case.

June 2010

- Examine the Mars Express PFS data, and re-evaluate Formisano et al. [2004] results on methane detection.

July - September 2010

- Perform a side-by-side spectroscopic comparison of the LHR and the high resolution Fourier transform spectrometer (figure 5.1) in their ability to detect the methane in the constructed ‘Martian’ gas cell. Determine if the LHR can identify the methane as well, or better than, the conventional FTS. Determine the minimum resolution required to resolve the fundamental methane bands using both instruments.

October 2010 - Spring 2011

- Further refine the Mars atmospheric model in RADTRANS.
- Make further develops to the LHR and make considerations for miniaturisation of the instrument. A significant goal to achieve at this point would be reaching Technology Readiness Level (TRL) 5. Development of the instrument for the study of the Martian atmosphere.
- Consider the potential for the instrument to be involved in a mission to Mars. The Mars Science Orbiter (MSO) mission in 2016 will perform a survey of the planet before the launch of ExoMars scheduled for 2018. There are currently plans to fly a high resolution FTS onboard. The LHR has advantages over this type of instrument, such as weight and size. Need to prove that the LHR is better choice over the currently planned spectrometer.

January 2011 - September 2011

- Write-up of thesis.

Acknowledgments

I would like start by thanking my supervisors, Dr. Neil Bowles for all the help and guidance he has given me over the past year, and Dr. Kevin Smith of the Rutherford Appleton Laboratory (RAL). I would like to express my appreciation to Nick Teanby for his advice on running RADTRANS simulations. Thanks goes to Gary Williams for his technical support during the time I have spent working at the Molecular Spectroscopy Facility (MSF) at RAL. I would also like to thank those whom for the last year I have shared an office with; David and Jo. Both provided invaluable advice during times of IDL programming frustration, and David for our discussions pertaining to Martian water vapour. I am also grateful to Ramin for our conversations relating to the problem of dust on Mars. A thank you goes to the Science and Technology Facilities Council (STFC) for funding this work at AOPP and RAL.

Bibliography

The HITRAN Database. URL <http://www.cfa.harvard.edu/hitran>.

Wolfram Research: Eric Weisstein's World of Physics. URL <http://scienceworld.wolfram.com/physics>.

RADTRANS Manual. Atmospheric, Oceanic and Planetary Physics, University of Oxford.

S. K. Atreya, A.-S. Wong, N. O. Renno, W. M. Farrell, G. T. Delory, D. D. Sentman, S. A. Cummer, J. R. Marshall, S. C. R. Rafkin, and D. C. Catling. Oxidant Enhancement in Martian Dust Devils and Storms: Implications for Life and Habitability. *Astrobiology*, 6:439–450, June 2006. doi: 10.1089/ast.2006.6.439.

S. K. Atreya, P. R. Mahaffy, and A.-S. Wong. Methane and related trace species on Mars: Origin, loss, implications for life, and habitability. *Planetary and Space Science*, 55:358–369, February 2007. doi: 10.1016/j.pss.2006.02.005.

C. N. Banwell and E. M. McCash. *Fundamentals of Molecular Spectroscopy: Fourth Edition*. McGraw-Hill, 1994.

R. Beer. *Remote Sensing by Fourier Transform Spectroscopy*. Wiley-Interscience, 1992.

P. J. Boston, M. V. Ivanov, and C. P. McKay. On the possibility of chemosynthetic ecosystems in subsurface habitats on Mars. *Icarus*, 95:300–308, February 1992. doi: 10.1016/0019-1035(92)90045-9.

N. E. Bowles. *Infrared Spectroscopy to Support Measurement of the Atmosphere of the Planet Jupiter*. PhD thesis, Atmospheric, Oceanic, and Planetary Physics, Department of Physics, Clarendon Laboratory, University of Oxford, 2003.

Bruker IFS 125HR User Manual. Bruker Optics, 2006.

J. W. Chamberlain and M. B. McElroy. Martian Atmosphere: The Mariner Occultation Experiment. *Science*, 152:21–25, April 1966. doi: 10.1126/science.152.3718.21.

R. J. Cicerone and R. S. Oremland. Biogeochemical aspects of atmospheric methane. *Global Biogeochemical Cycles*, 2:299–327, 1988. doi: 10.1029/GB002i004p00299.

- R. T. Clancy, B. J. Sandor, M. J. Wolff, P. R. Christensen, M. D. Smith, J. C. Pearl, B. J. Conrath, and R. J. Wilson. An intercomparison of ground-based millimeter, MGS TES, and Viking atmospheric temperature measurements: Seasonal and interannual variability of temperatures and dust loading in the global Mars atmosphere. *Journal of Geophysical Research*, 105:9553–9572, April 2000. doi: 10.1029/1999JE001089.
- S. M. Clifford. The role of thermal vapor diffusion in the subsurface hydrologic evolution of Mars. *Geophysical Research Letters*, 18:2055–2058, November 1991. doi: 10.1029/91GL02469.
- B. J. Conrath. Thermal structure of the Martian atmosphere during the dissipation of the dust storm of 1971. *Icarus*, 24:36–46, January 1975. doi: 10.1016/0019-1035(75)90156-6.
- M. Endemann. MIPAS Instrument Concept and Performance. *European Symposium on Atmospheric Measurements from Space*, January 1999.
- J. Faist, F. Capasso, D. L. Sivco, C. Sirtori, A. L. Hutchinson, and A. Y. Cho. Quantum Cascade Laser. *Science*, 264:553–556, April 1994. doi: 10.1126/science.264.5158.553.
- W. M. Farrell, G. T. Delory, and S. K. Atreya. Martian dust storms as a possible sink of atmospheric methane. *Geophysical Research Letters*, 33:21203–+, November 2006. doi: 10.1029/2006GL027210.
- K. Fast, T. Kostiuk, F. Espenak, J. Annen, D. Buhl, T. Hewagama, M. F. A’Hearn, D. Zipoy, T. A. Livengood, G. Sonnabend, and F. Schmülling. Ozone abundance on Mars from infrared heterodyne spectra. I. Acquisition, retrieval, and anticorrelation with water vapor. *Icarus*, 181:419–431, April 2006a. doi: 10.1016/j.icarus.2005.12.001.
- K. Fast, T. Kostiuk, T. Hewagama, M. F. A’Hearn, T. A. Livengood, S. Lebonnois, and F. Lefèvre. Ozone abundance on Mars from infrared heterodyne spectra. II. Validating photochemical models. *Icarus*, 183:396–402, August 2006b. doi: 10.1016/j.icarus.2006.03.012.
- F. Forget, F. Costard, and P. Lognonne. *Planet Mars: Story of Another World*. Springer Praxis, 2008.
- V. Formisano, S. Atreya, T. Encrenaz, N. Ignatiev, and M. Giuranna. Detection of Methane in the Atmosphere of Mars. *Science*, 306:1758–1761, December 2004. doi: 10.1126/science.1101732.
- V. Formisano, F. Angrilli, G. Arnold, S. Atreya, G. Bianchini, D. Biondi, A. Blanco, M. I. Blecka, A. Coradini, L. Colangeli, A. Ekonomov, F. Esposito, S. Fonti, M. Giuranna, D. Grassi, V. Gnedykh, A. Grigoriev, G. Hansen, H. Hirsh, I. Khatuntsev, A. Kiselev, N. Ignatiev, A. Jurewicz, E. Lellouch, J. Lopez Moreno, A. Marten, A. Mattana, A. Maturilli, E. Mencarelli, M. Michalska, V. Moroz, B. Moshkin, F. Nespoli, Y. Nikolsky, R. Orfei, P. Orleanski, V. Orofino, E. Palomba, D. Patsaev, G. Piccioni, M. Rataj, R. Rodrigo, J. Rodriguez, M. Rossi, B. Saggin, D. Titov, and L. Zasova.

- The Planetary Fourier Spectrometer (PFS) onboard the European Mars Express mission. *Planetary and Space Science*, 53:963–974, August 2005. doi: 10.1016/j.pss.2004.12.006.
- P. Forster, V. Ramaswamy, P. Artaxo, T. Berntsen, R. Betts, D. W. Fahey, J. Haywood, D. C. Lowe, G. Myhre, J. Nganga, R. Prinn, G. Raga, M. Schulz, and R. Van Dorland. Changes in Atmospheric Constituents and in Radiative Forcing. In: *Climate Change 2007: The Physical Science Basis. Contribution of Working Group I to the Fourth Assessment Report of the Intergovernmental Panel on Climate Change*. Technical report, Intergovernmental Panel on Climate Change, 2007.
- T. Fouchet, E. Lellouch, N. I. Ignatiev, F. Forget, D. V. Titov, M. Tschimmel, F. Montmessin, V. Formisano, M. Giuranna, A. Maturilli, and T. Encrenaz. Martian water vapor: Mars Express PFS/LW observations. *Icarus*, 190:32–49, September 2007. doi: 10.1016/j.icarus.2007.03.003.
- I. Fung, M. Prather, J. John, J. Lerner, and E. Matthews. Three-dimensional model synthesis of the global methane cycle. *Journal of Geophysical Research*, 96:13033–+, July 1991. doi: 10.1029/91JD01247.
- T. P. Greene, A. T. Tokunaga, D. W. Toomey, and J. B. Carr. CSHELL: a high spectral resolution 1-5 μm cryogenic echelle spectrograph for the IRTF. In A. M. Fowler, editor, *Society of Photo-Optical Instrumentation Engineers (SPIE) Conference Series*, volume 1946 of *Society of Photo-Optical Instrumentation Engineers (SPIE) Conference Series*, pages 313–324, October 1993.
- R. A. Hanel, B. J. Conrath, D. E. Jennings, and R. E. Samuelson. *Exploration of the Solar System by Infrared Remote Sensing: Second Edition*. April 2003.
- K. H. Hinkle, R. W. Cuberly, N. A. Gaughan, J. B. Heynssens, R. R. Joyce, S. T. Ridgway, P. Schmitt, and J. E. Simmons. Phoenix: a cryogenic high-resolution 1 to 5 μm infrared spectrograph. In A. M. Fowler, editor, *Society of Photo-Optical Instrumentation Engineers (SPIE) Conference Series*, volume 3354 of *Society of Photo-Optical Instrumentation Engineers (SPIE) Conference Series*, pages 810–821, August 1998.
- D. Horn, J. M. McAfee, A. M. Winer, K. C. Herr, and G. C. Pimentel. The Composition of the Martian Atmosphere: Minor Constituents. *Icarus*, 16: 543–+, June 1972. doi: 10.1016/0019-1035(72)90101-7.
- P. G. J. Irwin, S. B. Calcutt, and F. W. Taylor. Radiative transfer models for Galileo NIMS studies of the atmosphere of Jupiter. *Advances in Space Research*, 19:1149–1158, May 1997. doi: 10.1016/S0273-1177(97)00266-4.
- A. Kliore. The Mars reference atmosphere. *Advances in Space Research*, 2, 1982.
- T. Kostiuk and M. J. Mumma. Remote sensing by IR heterodyne spectroscopy. *Applied Optics*, 22:2644–2654, September 1983.
- V. A. Krasnopolsky. Uniqueness of a solution of a steady state photochemical problem: Applications to Mars. *Journal of Geophysical Research*, 100:3263–3276, February 1995. doi: 10.1029/94JE03283.

- V. A. Krasnopolsky. Some problems related to the origin of methane on Mars. *Icarus*, 180:359–367, February 2006. doi: 10.1016/j.icarus.2005.10.015.
- V. A. Krasnopolsky, G. L. Bjoraker, M. J. Mumma, and D. E. Jennings. High-resolution spectroscopy of Mars at 3.7 and 8 μm : A sensitive search for H_2O_2 , H_2CO , HCl, and CH_4 , and detection of HDO. *Journal of Geophysical Research*, 102:6525–6534, March 1997. doi: 10.1029/96JE03766.
- V. A. Krasnopolsky, J. P. Maillard, and T. C. Owen. Detection of methane in the martian atmosphere: evidence for life? *Icarus*, 172:537–547, December 2004. doi: 10.1016/j.icarus.2004.07.004.
- F. Lefèvre and F. Forget. Observed variations of methane on Mars unexplained by known atmospheric chemistry and physics. *Nature*, 460:720–723, August 2009. doi: 10.1038/nature08228.
- E. Lellouch, T. Encrenaz, T. de Graauw, S. Erard, P. Morris, J. Crovisier, H. Feuchtgruber, T. Girard, and M. Burgdorf. The 2.4–45 μm spectrum of Mars observed with the infrared space observatory. *Planetary and Space Science*, 48:1393–1405, October 2000.
- C. B. Leovy, G. A. Briggs, A. T. Young, B. A. Smith, J. B. Pollack, E. N. Shipley, and R. L. Wildey. The Martian Atmosphere : Mariner 9 Television Experiment Progress Report (A 4.5). *Icarus*, 17:373–+, October 1972. doi: 10.1016/0019-1035(72)90006-1.
- S. R. Lewis, M. Collins, P. L. Read, F. Forget, F. Hourdin, R. Fournier, C. Hourdin, O. Talagrand, and J.-P. Huot. A climate database for Mars. *Journal of Geophysical Research*, 104:24177–24194, October 1999. doi: 10.1029/1999JE001024.
- R. Lolachi. Hunting for Water Vapour with MCS: AOPP Second Year Report. Technical report, 2008.
- J. R. Lyons, C. E. Manning, and F. Nimmo. Formation of methane on Mars by fluid-rock interaction in the crust. *AGU Fall Meeting Abstracts*, pages A4+, December 2005.
- W. C. Maguire. Martian isotopic ratios and upper limits for possible minor constituents as derived from Mariner 9 infrared spectrometer data. *Icarus*, 32:85–97, September 1977. doi: 10.1016/0019-1035(77)90051-3.
- E. Matthews and I. Fung. Methane Emission From Natural Wetlands: Global Distribution, Area, and Environmental Characteristics of Sources. *Global Biogeochemical Cycles*, 1:61, 1987.
- M. D. Max and S. M. Clifford. The state, potential distribution, and biological implications of methane in the Martian crust. *Journal of Geophysical Research*, 105:4165–4172, February 2000. doi: 10.1029/1999JE001119.
- R. T. Menzies. *Laser heterodyne detection techniques*, pages 297–353. 1976.
- M. V. Migeotte. Spectroscopic evidence of methane in the earth’s atmosphere. *Phys. Rev.*, 73(5):519–520, Mar 1948. doi: 10.1103/PhysRev.73.519.2.

- M. J. Mumma, R. E. Novak, M. A. DiSanti, B. P. Bonev, and N. Dello Russo. Detection and Mapping of Methane and Water on Mars. In *Bulletin of the American Astronomical Society*, volume 36 of *Bulletin of the American Astronomical Society*, pages 1127–+, November 2004.
- M. J. Mumma, G. L. Villanueva, R. E. Novak, T. Hewagama, B. P. Bonev, M. A. DiSanti, A. M. Mandell, and M. D. Smith. Strong Release of Methane on Mars in Northern Summer 2003. *Science*, 323:1041–, February 2009. doi: 10.1126/science.1165243.
- H. Nair, M. Allen, A. D. Anbar, Y. L. Yung, and R. T. Clancy. A photochemical model of the martian atmosphere. *Icarus*, 111:124–150, September 1994. doi: 10.1006/icar.1994.1137.
- C. Oze and M. Sharma. Have olivine, will gas: Serpentinization and the abiogenic production of methane on Mars. *Geophysical Research Letters*, 32: 10203–+, May 2005. doi: 10.1029/2005GL022691.
- P. L. Read and S. R. Lewis. *The Martian Climate Revisited: Atmosphere and Environment of a Desert Planet*. Springer Praxis, 2004.
- L. S. Rothman, D. Jacquemart, A. Barbe, D. Chris Benner, M. Birk, L. R. Brown, M. R. Carleer, C. Chackerian, K. Chance, L. H. Coudert, V. Dana, V. M. Devi, J.-M. Flaud, R. R. Gamache, A. Goldman, J.-M. Hartmann, K. W. Jucks, A. G. Maki, J.-Y. Mandin, S. T. Massie, J. Orphal, A. Perrin, C. P. Rinsland, M. A. H. Smith, J. Tennyson, R. N. Tolchenov, R. A. Toth, J. Vander Auwera, P. Varanasi, and G. Wagner. The HITRAN 2004 molecular spectroscopic database. *Journal of Quantitative Spectroscopy and Radiative Transfer*, 96:139–204, December 2005. doi: 10.1016/j.jqsrt.2004.10.008.
- F. S. Rowland. Methane and chlorocarbons in the earth’s atmosphere. *Origins of Life*, 15:279–297, 1985.
- C. Sagan and R. A. Bagnold. Fluid transport on earth and aeolian transport on Mars. *Icarus*, 26:209–218, October 1975. doi: 10.1016/0019-1035(75)90080-9.
- M. D. Smith. The annual cycle of water vapor on Mars as observed by the Thermal Emission Spectrometer. *Journal of Geophysical Research (Planets)*, 107:5115–+, November 2002. doi: 10.1029/2001JE001522.
- M. D. Smith. Interannual variability in TES atmospheric observations of Mars during 1999-2003. *Icarus*, 167:148–165, January 2004. doi: 10.1016/S0019-1035(03)00287-2.
- M. C. Teich. Laser Heterodyning. *Journal of Modern Optics*, 32:1015–1021, September 1985. doi: 10.1080/713821834.
- O. B. Toon, J. B. Pollack, and C. Sagan. Physical properties of the particles composing the Martian dust storm of 1971-1972. *Icarus*, 30:663–696, April 1977. doi: 10.1016/0019-1035(77)90088-4.
- D. Weidmann and G. Wysocki. High-resolution broadband ($>100\text{ cm}^{-1}$) infrared heterodyne spectro-radiometry using an external cavity quantum cascade laser. *Optics Express*, 17:248–+, December 2008. doi: 10.1364/OE.17.000248.

- D. Weidmann, W. J. Reburn, and K. M. Smith. Ground-based prototype quantum cascade laser heterodyne radiometer for atmospheric studies. *Review of Scientific Instruments*, 78(7):073107–+, July 2007a. doi: 10.1063/1.2753141.
- D. Weidmann, W. J. Reburn, and K. M. Smith. Retrieval of atmospheric ozone profiles from an infrared quantum cascade laser heterodyne radiometer: results and analysis. *Applied Optics*, 46:7162–7171, October 2007b. doi: 10.1364/AO.46.007162.
- B. P. Weiss, Y. L. Yung, and K. H. Neelson. Atmospheric energy for subsurface life on Mars? *Proceedings of the National Academy of Science*, 97:1395–1399, February 2000. doi: 10.1073/pnas.030538097.
- G. Wiedemann, D. Deming, and G. Bjoraker. A Sensitive Search for Methane in the Infrared Spectrum of τ Bootis. *Astrophysical Journal*, 546:1068–1074, January 2001. doi: 10.1086/318316.
- D. R. Williams. NASA Mars Fact Sheet, September 2004. URL <http://nssdc.gsfc.nasa.gov/planetary/factsheet/marsfact.html>.
- M. J. Wolff and R. T. Clancy. Constraints on the size of Martian aerosols from Thermal Emission Spectrometer observations. *Journal of Geophysical Research (Planets)*, 108:5097–+, September 2003. doi: 10.1029/2003JE002057.
- M. J. Wolff, M. D. Smith, R. T. Clancy, N. Spanovich, B. A. Whitney, M. T. Lemmon, J. L. Bandfield, D. Banfield, A. Ghosh, G. Landis, P. R. Christensen, J. F. Bell, and S. W. Squyres. Constraints on dust aerosols from the Mars Exploration Rovers using MGS overflights and Mini-TES. *Journal of Geophysical Research (Planets)*, 111:12–+, December 2006. doi: 10.1029/2006JE002786.
- A.-S. Wong, S. K. Atreya, and T. Encrenaz. Chemical markers of possible hot spots on Mars. *Journal of Geophysical Research (Planets)*, 108:5026–+, April 2003. doi: 10.1029/2002JE002003.

Appendix A

Equations

Lorentz Half-Width

$$\alpha_L = \alpha_L^0 \frac{P}{P_0} \left(\frac{T_0}{T} \right)^{\frac{1}{2}}$$

where P is the atmosphere pressure on Mars at a defined altitude, P₀ is the surface pressure on Earth, T is the temperature on Mars at a defined altitude, T₀ is the temperature on Earth, and n is the pressure broadening temperature dependence index. $\alpha_L^0 = 0.085 \text{ cm}^{-1}$ [The HITRAN Database].

Doppler Half-Width

$$\alpha_D = \frac{v_0}{c} \sqrt{\frac{2RT}{m}}$$

where R is the gas constant (8.314 J K⁻¹ mol⁻¹), T is the temperature and m is the molar mass of the molecule. CH₄ molar mass = 16.0426 g/mole.

Appendix B

A Summary of Mars Missions

NASA Mariner Probes

- **Mariner 3** - Failed - Lost en route
- **Mariner 4** - Launched: November 28th, 1964. Reached Mars: July 14th, 1965. Mars pass at 9,850km. Sent back 22 photos of the Martian surface (Southern Hemisphere). Observed no canals or Martians, just craters. Indirect analysis of the atmosphere indicated a surface pressure of less than 7mbar.
- **Mariner 6 & 7** - 1969 - They were identical spacecraft sent to flyby Mars in order to collect data about the surface and atmosphere of Mars. Made the first observations of the surface in IR and UV. Together, they returned over 200 images of the Martian surface. Most famously, Mariner 7 took the first close-up images of the deep valley, which now bears its name, Valles Marineris.
- **Mariner 8** - Failed - Launch failure
- **Mariner 9** - Launched: May 30th, 1971. Reached Mars: November 14th, 1971 - First artificial satellite of a planet other than Earth. Carried out a complete photographic survey of the Martian surface. Sent back over 7,000 photos. Also took the first detailed pictures of moons Phobos and Deimos.

NASA Viking Probes

- **Viking 1** - Launched: August 20th, 1975. Reached Mars: June 19th, 1976. Orbiter: Searched for ideal landing site for Lander. Completed 1485 orbits. Instruments: Cameras, IR radiometer, water vapour detector. Lander: Landed July 20th, 1976 at Chryse Planitia.
- **Viking 2** - Launched: September 9th, 1975. Reached Mars: August 7th, 1976. Orbiter: Returned almost 16,000 images in about 700 – 706 orbits around Mars. Lander: Landed the other side of the planet to Viking 1 at Utopia Planitia.

NASA Mars Orbiters

- **Mars Observer** - Launched: September 25th, 1992 - Failed to enter Mars orbit, communication lost - Mission: to study the geoscience and climate of Mars.
- **Mars Global Surveyor** - Entered Orbit: September 12th, 1997 - Mission: to study magnetic field, gravity, topography, ionosphere electron densities. Visible and IR imaging.
- **Mars Climate Orbiter** - Entered Orbit: September 23rd, 1999 - Failed - Lost during orbital insertion.
- **Mars Odyssey** - Entered Orbit: October 24th, 2001 - Mission: to study surface mineralogy and ionizing radiation. IR Imaging.
- **Mars Reconnaissance Orbiter** - Entered Orbit: March 10th, 2006 - Mission: to study temperature, water vapour, dust and atmospheric clouds. Visible, IR and radar imaging of upper sub-surface.

NASA Mars Landers

- **Mars Pathfinder** - Landed July 4th 1997 - Mission: to study rock mineralogy and magnetism. Planetary pressure, temperature, wind and rotation. Panoramic imaging.
- **Mars Polar Lander** - Failed - Crash landed - December 3rd, 1999 - Partner probe: Mars Climate Orbiter.
- **Mars Exploration Rovers:**
 - **Spirit** - Landed January 3rd, 2004
 - **Opportunity** - Landed January 28th, 2004 Mission: Mineralogical investigation, rock and texture study and dust study.
- **Phoenix** - Landed May 25th, 2008 - Mission: to study the Martian 'Arctic'. Soil collection by robotic boom, chemical analysis, meteorology and imaging.
- **Mars Science Laboratory** - Landing projected for autumn, 2012 - Mission: long distance exploration, imaging and detailed analysis of samples.

ESA Missions

- **Mars Express** - Launched: June 2nd, 2003 – Mission: high-resolution imaging and mineralogical mapping of the surface, radar sounding of the subsurface structure down to the permafrost, precise determination of the atmospheric circulation and composition, and study of the interaction of the atmosphere with the interplanetary medium.
 - Lander: **Beagle 2** - Failed - Crash landed - December 25th, 2003

JAXA (Japan Aerospace Exploration Agency)

- **Nozomi** - Launched: July 3rd, 1998 - Lost en route - A malfunctioning valve during the Earth swing-by resulted in a loss of fuel and left the spacecraft with insufficient acceleration to reach its planned trajectory.

USSR & Russian Mars Probes

- **Marsnik 1** - Launched: October 10th, 1960 - Failed - Launch failure
- **Mars 1** - Launched: November 1st, 1962 - Failed - Lost en route
- **Kosmos 419** - Launched: May 10th, 1971 - Failed en route (did not escape Earth orbit).
- **Mars 2** - Launched: May 19th, 1971. Reached Mars: November 27th, 1971. Orbiter: Completed 362 orbits and sent back images. Lander: Crashed
- **Mars 3** - Launched: May 28th, 1971. Reached Mars: December 2nd, 1971. Orbiter: Suffered from a partial loss of fuel and did not have enough to put itself into a planned 25 hour orbit. The engine instead performed a truncated burn to put the spacecraft into a long 12 day, 19 hour period orbit about Mars. Lander: Landed on the Martian surface but transmitted for only 14.5 seconds.
- **Mars 4** - Launched: July 21st, 1973. Reached Mars: February 10th, 1974. Failed to enter Mars orbit.
- **Mars 5** - Launched: July 25th, 1973. Reached Mars: February 12th, 1974. Completed 22 orbits and then ceased transmitting.
- **Mars 6** - Launched: August 5th, 1973. Reached Mars: March 12th, 1974. Landed but lost contact with Earth. The descent module transmitted 224 seconds of data before transmissions ceased, the first data returned from the atmosphere of Mars.
- **Mars 7** - Launched: August 9th, 1973. Reached Mars: March 9th, 1974. Went off course and was lost in space.
- **Phobos 1** - 1988 - Failed - Lost en route.
- **Phobos 2** - 1988 - Gathered data and took photographs of Mars and Phobos from orbit. However, it failed before launching two Phobos landing probes.
- **Mars 96** - 1996 - Launch failure.